Transient stages during the chemical vapour deposition of silicon carbide from CH3SiCl3/H2: impact on the physicochemical and interfacial properties of the coatings

Georges Chollon, Francis Langlais, Maud Placide, Patrick Weisbecker

Transient Stages in the CVD of Silicon Carbide from CH_3SiCl_3/H_2: Impact on the Physicochemical and Interfacial Properties of the Coatings

Georges CHOLLON*, Francis LANGLAIS, Maud PLACIDE, Patrick WEISBECKER
Laboratoire des Composites Thermostructuraux (CNRS, SPS, CEA, UB1)
3, allée de La Boétie, 33600 PESSAC, FRANCE
* Corresponding author. Tel: 33 5 56 84 47 27, Fax: 33 5 56 84 12 25, E-mail: chollon@lcts.u-bordeaux1.fr

Abstract

Transient CVD experiments were produced from CH_3SiCl_3(MTS)/H_2 mixtures, by varying linearly as a function of time the deposition temperature or the initial gas flow rates (Q_{MTS} or Q_{H2}). The consequences on the composition of the gas phase, the deposition rates, and the physicochemical properties of the transient coating layers (φ_{Tr}) have been respectively examined by in situ FTIR, thermogravimetric analyses, Raman spectroscopy and TEM. Finally, the adhesion of SiC/φ_{Tr}/SiC bilayers, obtained using various transient stages, was investigated by scratch testing.

For transient stages resulting from a decrease of Q_{MTS} or T, crystallized or amorphous silicon can be co-deposited, due the higher reactivity of $SiCl_x$ radicals as compared to hydrocarbons. In this case, the continuous covalent bonding through the Si-rich interfacial layers preserves the strong adhesion between the two stoichiometric layers.

Transient stages resulting from a decrease of Q_{H2} close to zero eventually lead to the co-deposition of anisotropic carbon, due to the formation of unsaturated hydrocarbons in the gas phase. The interfacial layers with the largest thicknesses and including a continuous anisotropic carbon interlayer lead to poor adhesion properties. Conversely, thin and discontinuous carbon-rich interfacial layers do not affect the interfacial properties significantly.

Highlights

- Systematic investigations of various CVD transient stages: f(T or H_2/CH_3SiCl_3)
- Correlation between changes of CVD parameters and in situ gas phase composition
- Correlation between CVD parameters and deposition rate
- Correlation between CVD parameters and nature of the gradient Si-C coatings

- Synthesis of SiC/φ_{Tr}/SiC bilayers with various transient interphases (φ_{Tr})
- Assessment of SiC/φ_{Tr}/SiC bilayers adhesion properties by scratch testing

Keywords

CVD, Silicon Carbide, Transient Stages, FTIR, Kinetics, Microstructure, Adhesion, Scratch Testing

1 Introduction

The need of refractory materials for uses in particularly harsh conditions has led to significant advances in many fields of the materials science [1]. These high temperature components are usually coated to protect them against corrosion, intense heat fluxes or wear. Silicon carbide (SiC) is a coating material of choice because of its exceptional properties (chemical inertness, thermal conductivity, hardness…). SiC coatings are employed for instance to protect chemical reactors, space mirrors, thermostructural composite materials or the fission fuel containers of the future nuclear reactors. Chemical vapour deposition (CVD) is the most often used technique to deposit SiC coatings, because it allows an excellent control of their composition, structure and thickness uniformity. An important precaution during the synthesis of CVD coatings is the control of the adherence of the coating to the substrate or between different layers, in a multilayer coating.

When a SiC coating is synthesized by CVD, the experimental parameters (temperature, pressure, gas flow rates) vary significantly before and after steady state deposition, at the beginning and at the end of the process. The conditions may also be altered accidentally in a variable extent during a steady phase of deposition. These CVD *transient stages* may result in the deposition of superficial or confined layers having singular chemical and structural properties. When a transient stage occurs, for instance, during the starting up of the process, before the regular deposition stage, or between two steady phases, an interfacial layer is formed that can sometimes lead to the debonding of the outer SiC layer [2]. The objective of the present work is to reproduce, in a controlled manner, different types of transient stages, and to examine their consequences on the adhesion between two SiC layers. By analogy with ceramic matrix composites (CMC), where this term refers to the intermediate layer(s) between a fibre and the matrix [3], we will use interphase or *transient interphases* (φ_{Tr}) to define an interfacial layer resulting from a transient deposition stage which is covered with a SiC outer layer. Yet, the context of this work is not to develop new interphases, aiming at the proper deviation of cracks, as in CMC [3], but rather to understand the formation of transient interphases in certain CVD conditions and eventually the reason why they can cause the debonding of the outer coating.

Methyltrichlorosilane (CH_3SiCl_3, MTS) diluted in hydrogen (H_2) is the most commonly used single-source SiC precursor, mainly because of its composition ($Si/C_{at.} = 1$), vapour pressure, thermal stability, but also for the high properties of the resulting coatings. A considerable amount of work has been conducted on the CVD from MTS/H_2 mixtures for more than 40 years [2, 4-49]. It rapidly appeared from these studies that the homogeneous chemistry resulting from the thermal

decomposition of MTS is particularly complex and plays a critical part in the deposition process [6-12]. From the early times to very recently, theoretical -thermodynamic and kinetic- approaches have been proposed to describe the homogeneous reactions taking place in the reactor and the nature of the gas species, particularly of the effective precursors of the Si-C solid [13-21]. In parallel, experimental studies have been conducted to investigate the influence of the CVD parameters on the growth rate [23-34, 36-46, 48-49], the composition of the gas phase (in situ or downstream of the reactor) [6-12, 48], the nature (i.e. the stoichiometry and the structure) of the deposited solid [10-11, 27, 30, 32, 34-35, 37-42, 45-49] and even its mechanical properties [22-23]. Several authors have even combined these various aspects to develop models to predict the growth rates [33, 36-37, 43, 45]. Some experimental results however, even when obtained at comparable deposition temperature, are sometimes scattered because of the very wide range of residence time (t_r) of the reactive gas mixture in the deposition chamber. This parameter, which controls the homogeneous reactions, is indeed strongly related to the various conditions of total pressure (reduced or atmospheric), gas flow and reactor geometry explored in these studies.

The present report considers only isothermal and low pressure-isobaric CVD, because these conditions are more suited to the industrial production of SiC-based coatings or composites, of large size and at large scale [50-51]. Even within these restricted conditions, the CVD from the MTS/H_2 system at constant T and P, and given initial gas phase composition (usually defined by the standard gas flow ratio $\alpha = Q_{H2}/Q_{MTS}$), has been extensively studied [25-26, 28-34, 37, 39-42]. The correlation between thermodynamic calculations, the monitoring of the gas species formed in the reactor, the growth kinetics and the characterization of the solid, has allowed proposing homogeneous and heterogeneous (adsorption, nucleation and growth) reaction mechanisms [30-31, 37].

If the present study can definitely rely on these previous works, the conditions of initial gas precursor composition and temperature encountered during typical transient stages can notably deviate from those already explored. It has been therefore necessary to complete these studies by investigating a more extended range of steady conditions and, particularly, of parameter α.

After this preliminary work on steady stage but non-conventional CVD conditions, the second part of the study is dedicated, properly speaking, to transient state CVD. Three types of transient stages have been considered consisting in decreasing respectively: (i) the temperature, (ii) the MTS flow rate and (iii) the H_2 flow rate. The consequences on the composition of the gas phase and the deposition kinetics have been respectively examined by in situ FTIR and thermogravimetric analyses. The chemical and structural properties of the resulting transient coatings have been

analysed in detail and correlated with the previous investigations on the homogeneous reactions and the deposition rates.

Finally, the adhesion of various SiC/φ_{Tr}/SiC bilayers (two adjacent SiC layers separated by a certain type of transient interphase φ_{Tr}), has been assessed using scratch testing. The results have been discussed on the basis of the CVD conditions and the chemical and structural properties of the interphase.

2 Experimental procedures

The CVD apparatus is shown in Fig. 1. It is a vertical hot wall reactor operating at reduced pressure. It consists of a silica tube (100 mm in inner diameter), heated in its central part by radio-frequency. The quasi-isothermal deposition zone (+/-5°C) is approximately 100 mm-long. The coatings were deposited on small pellets of single crystal silicon wafer (20x10x0.5 mm^3), previously cleaned in ethanol and heated under a pure H_2 flow before starting deposition.

All the coatings were prepared in conditions deviating more or less from the reference condition defined by: a total pressure P = 5 kPa, a temperature T = 1000°C, a precursor gas ratio α = 3 and a total gas flow rate Q_{tot} = 200 sccm. The whole range of conditions explored was: P = 5 or 10 kPa, T = 750-1050°C, α = 0-∞, Q_{tot} = 100-400 sccm.

A high sensitivity microbalance (BSetsys from Setaram) was connected to the top of the reactor, specifically for the in situ measurements of the deposition kinetics. The specimen was hung to the balance, allowing the acquisition of the deposition rate (in $mgmin^{-1}cm^{-2}$) at a given position in the hot zone of the reactor.

A Fourier-transform infrared (FTIR) spectrometer (Nicolet 550, run with OMNIC) was coupled to the CVD reactor [52]. The in situ detection of the reactants, intermediates and product species and a semi-quantitative analysis of the gas concentrations (peak areas) were performed in the transmission mode (the incident IR beam going axially through the reactor before reaching the HgCdTe detector).

The uniformity and the average chemical composition of the coatings (with an error of approximately ±2 at.%) were characterized by recording in-depth Auger electron spectroscopy (AES) concentration profiles (VG Microlab 310-F).

The morphology of the free surface and the fractured cross-section of the coatings was observed by field emission gun scanning electron microscopy (FEG-SEM, Hitachi S-4500).

X-ray diffraction (XRD, Siemens D5000, $\lambda_{Cu\text{-}K\alpha}$ = 0.1542 nm), Raman microspectroscopy (RMS, HORIBA Jobin Yvon, Labram HR, λ = 632.8 nm) and transmission electron microscopy (TEM, Philips, CM30SP) were used to identify crystalline phases in the coatings.

The SiC/φ_{Tr}/SiC bilayers were submitted to a scratch tester Tribotechnic Millenium 100. A diamond spherical indenter ($\varnothing$ = 200 μm) was used to scratch the surface of the specimen with a linearly increasing load (30 $Nmin^{-1}$, 5 $mmmin^{-1}$). The damaging of the specimen was detected from the acoustic emission (AE) signal recorded during the scratch testing, and from direct examinations of the scratched specimen. The occurrence of debonding of the outer SiC coating was confirmed by post-mortem SEM observations and laser profilometry analyses along the scratch path.

3 Results and discussion

3-1 CVD in steady state conditions

In this section, only the composition of the gas phase (obtained by in situ FTIR spectroscopy) and the properties of the coatings (composition, structure) have been investigated as a function of α, T and P. The peak areas of the characteristic gas species were recorded only in the steady state regime. This was easily ensured by checking the evolution of the IR spectrum versus time. The background IR spectrum was recorded in the same T and P conditions, but after the interruption of the MTS flow and the complete flushing of the gases by H_2. The AES and RMS analyses allowed local examination of the coating throughout its thickness. The Si/C atomic ratios and the Raman spectra are average information from uniform domains encountered along the depth profiles and corresponding to the steady stages. The deposition kinetics was not systematically investigated in the steady state regime. The deposition rate was assessed only during some specific slow-rate transient conditions (see section 3-2).

3-1-1 in situ FTIR analysis : influence of α and temperature

The gas phase was analysed in situ as function of temperature, at a total pressure of 5 kPa and for three different values of α (α = 0, 3 and 20). During the analysis in absorption, the IR beam goes through the reactor and therefore probes, simultaneously, the initial gas mixture at the inlet, the hot reactional zone and the product gases at the outlet.

For $\alpha = 3$ and $\alpha = 20$, the IR spectra are in agreement with previous studies on the CH_3SiCl_3/H_2 system [6-7, 9]. In addition to the initial CH_3SiCl_3 molecule, the product species detected are $HSiCl_3$, $SiCl_4$, CH_4 and HCl (see in Fig. 2 the spectrum recorded for P = 5kPa, T = 1000°C, $\alpha = 3$). To follow qualitatively the concentrations of these species as a function of the CVD conditions, one well-defined (non-saturating) band, characteristic of each species, was selected and integrated on the absorbance spectra. These IR features are illustrated in Fig. 2.

The variations of the peak areas as a function of temperature, (illustrated in Fig. 3 for P = 5kPa, $\alpha = 3$), clearly reveal the homogeneous decomposition of MTS starting at 750°C, to form the species mentioned above. The complete reaction mechanism is complex and has been often discussed by many authors [8, 10-12, 16, 18, 48]. Among the numerous elementary reactions reported, the few following probably account for the main consumption/formation of the species detected by FTIR in the gas phase (written in italic) [8]:

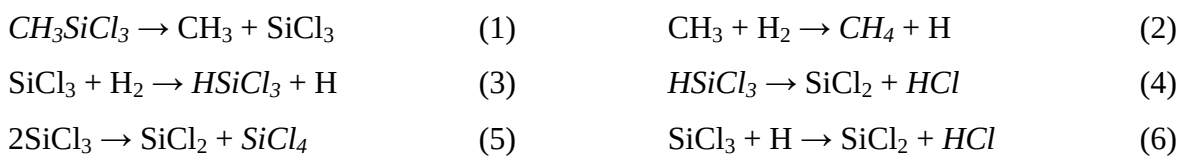

$$\textit{CH}_3\textit{SiCl}_3 \rightarrow CH_3 + SiCl_3 \quad (1) \qquad CH_3 + H_2 \rightarrow \textit{CH}_4 + H \quad (2)$$

$$SiCl_3 + H_2 \rightarrow \textit{HSiCl}_3 + H \quad (3) \qquad \textit{HSiCl}_3 \rightarrow SiCl_2 + \textit{HCl} \quad (4)$$

$$2SiCl_3 \rightarrow SiCl_2 + \textit{SiCl}_4 \quad (5) \qquad SiCl_3 + H \rightarrow SiCl_2 + \textit{HCl} \quad (6)$$

$SiCl_2$ is expected to be formed at high temperature from thermodynamic calculation [13, 16], and has already been observed by FTIR using the emission mode [6, 9, 19]. It was not detected here due to the spectral range limitation at low wave numbers ($\nu_{Si\text{-}Cl}$ = 490-510 cm^{-1}). The Si-Cl bond cleavage in $SiCl_2$ can also lead to Cl radicals that may react with H_2 or CH_4 to produce additional HCl. The decrease of the CH_4 and $SiCl_4$ concentrations, observed beyond 900°C in Fig. 3, is likely related to the heterogeneous chemical reactions (the deposition rate becoming significant at this temperature) [29]. These species, and/or more reactive intermediates (e.g., CH_3, $SiCl_3$, $SiCl_2$), indeed react on the reactor walls to form the SiC deposit. As expected from equations (2), (3), and the occurrence of Cl radicals in the hot zone of the reactor, the peak area ratios of $HSiCl_3/SiCl_4$, $CH_4/SiCl_4$ and $HCl/SiCl_4$, increase with α, i.e., with the amount of H_2 in the initial gas mixture.

For $\alpha = 0$ specifically, hydrocarbons (C_2H_4, C_2H_2 and C_6H_6) are also detected besides the above-mentioned molecules (see Fig. 4). The concentrations of the species resulting from the decomposition of MTS (e.g. CH_4, $SiCl_4$) strongly increase with the temperature up to 900°C for $\alpha = 0$ (see Fig. 5a), similarly as for $\alpha = 3$ (see Fig. 3) and $\alpha = 20$ (not shown). They decrease slightly beyond 900°C, probably due to their (or to other intermediates) consumption resulting from the deposition at high temperature [11, 29, 44]. The concentrations of C_2H_4 and C_6H_6, which are much

more reactive than CH_4, also decrease beyond 900°C (see Fig. 5b), suggesting an increase of the carbon content in the coatings. The MTS decomposition yield is improved when α decreases (compare Fig 3. and Fig. 5a), likely as a consequence of the increase of the partial pressure of MTS, favouring its dissociation [8, 12].

A particularly strong decrease of the $SiCl_4$ concentration is observed beyond 900°C for $\alpha = 20$. This suggests a heterogeneous consumption of the silicon-rich species at high temperature and, consequently, an increase of the silicon content of the coatings.

3-1-2 Composition and structure of the coatings: influence of α, temperature and total pressure

The elemental analysis of the coatings, deposited in various conditions, are plotted versus α in Fig. 6. The coating obtained in the standard condition (T = 1000°C, P = 5kPa and $\alpha = 3$) has a composition close to the stoichiometry. The Raman spectrum obtained from the same specimen shows the two optical phonons (longitudinal LO and transverse TO at about 700 and 1000 cm^{-1} respectively), typical of the SiC crystalline phases (see Fig. 7) [53]. Their important bandwidth and the presence of intense acoustic phonons (below 600 cm^{-1}) reveal a poor structural organization (with nanometre-size SiC grains) [47, 54-55]. The coatings do not contain a significant amount of free silicon (recognizable by a sharp peak at 520 cm^{-1} or a broad band around 480 cm^{-1}, depending on its crystalline state) and are totally free of a carbon excess (characterized by broad D and G bands at 1350 and 1600 cm^{-1}) [47, 54-55]. Fig 8a shows that the outer surface morphology of the coatings (as observed by SEM) is smooth and the fracture surface is typical of a fine microstructure. The TEM analyses (see the selected area electronic diffraction pattern (SAED) and SiC_{111} dark field in Fig. 8b-c) indicate the presence of the cubic SiC polytype (3C or β) in the form of nanometre-sized grains (3nm in average), with no preferential orientation.

Previous kinetic/physicochemical studies have shown that such a fine microstructure/texture is not typical of a growth regime limited by mass transfer (MTR), which is generally observed at high temperature (T > 1000°C). It is not characteristic of a limitation by chemical reactions (CRR) either, as such a regime rather applies at medium temperature (T < 950°C) and low pressure ($P \leq 5$ kPa) [28-32]. Both MTR and CRR regimes (the former particularly) indeed generally lead to textured coatings, with columnar and submicrometre-sized grains. A small SiC grain size is often associated with co-deposited silicon, such a microstructure being generally encountered for high pressures and α ratios, far apart from the current P = 5 kPa and $\alpha = 3$ values [32]. The “standard” microstructure

might result from a peculiar growth regime limited by the adsorption of chlorine-containing species such as HCl [29]. This regime, observed at temperatures of about 1000°C and pressures of 5-15 kPa, was indeed found to lead to smaller grain size than low-pressure CRR [32].

For a pressure of 5 kPa, a temperature of 1010°C and for $\alpha < 0.5$, the chemical and structural analyses (shown in Fig. 6 and 7a respectively) clearly show that the coatings contain free carbon in a quantity increasing when α decreases. As already suggested by the FTIR analyses, revealing the presence of hydrocarbons in the gas phase, the Si/C_{at} ratio decreases and the D and G bands (characteristic of sp^2 carbon) appear on the Raman spectra, with intensities increasing when α decreases from 1 down to 0 (a decrease of the total pressure or a dilution in argon was applied in a few cases to avoid the condensation of MTS for the lowest dilution in H_2. For $1 \leq \alpha \leq 20$, the Raman spectra shown in Fig. 7a indicate that the coatings remain stoichiometric but the change in the SiC feature bandwidth reveals an improvement of the crystalline state (i.e. an increase of the average grain size and/or a reduction of structural defects) when α diminishes.

For a common value of α, the decrease of temperature (from 1010 to 940°C) and the increase of the total pressure (from 5 to 10 kPa) both result in a much higher silicon concentration in the coatings. The change of the Si/C_{at} ratio and the RMS analyses confirm the presence of free silicon, in a quantity increasing with parameter α, and with a structure either amorphous or partially crystalline, depending on the deposition temperature. The increase of the total pressure simultaneously reduces the reactivity of the carbon species (by promoting the conversion of CH_3 into CH_4) and improves the reactivity of the silicon-containing species (e.g. by favouring the formation of $SiCl_2$) [30, 32]. Furthermore, at high pressure (P = 10 kPa) and medium temperature (≈ 950°C), the increase of the H_2 concentration in the gas mixture promotes the reduction of $SiCl_2$, i.e., the co-deposition of free silicon, while simultaneously it facilitates the formation of CH_4, inhibiting the deposition of carbon. The deposition regime is of the high-pressure RCC type and characterized by a strong dependence on the MTS partial pressure [28-32].

3-2 CVD in transient conditions

CVD experiments were carried out in transient conditions, by varying linearly as a function of time, at different rates, Q_{MTS}, Q_{H2} or T, from its standard value. In this case, an in situ time-resolved FTIR analysis was achieved to correlate the composition of the gas phase with the chemical and structural properties of the deposited solid. The deposition rate was also recorded in situ versus time, by

hanging the substrate to the microbalance. The instant deposition rate can be accurately correlated with the changes of the composition and the structure through the "transient coatings" (φ_{Tr}).

3-2-1 Transient deposition by a decrease of temperature

The transient deposition stage consists in this case in decreasing the temperature from about 1010°C, all the other parameters remaining unchanged (P = 5 kPa, α = 3). The analysis of the gas phase was achieved continuously versus temperature with a constant cooling rate (-8°Cmin^{-1}). First of all, temperature measurements were carried out under a pure H_2 flow, the end of a thin thermocouple being attached to a substrate installed in the centre of the furnace. These experiments confirmed that such a heating rate allowed the system to reach a quasi-steady state temperature distribution (i.e., between the hot reactor walls, the gas phase and the substrate). The peak area values for the different species are plotted versus time and temperature in Fig. 9. Their behaviour is similar to that observed in standard steady state conditions (see §3-1-1 and Fig. 3). The profiles shown in Fig. 9 were normalized in order to better appraise the concentration changes as a function of temperature. From 1010 to 750°C, the MTS relative intensity increases rapidly with decreasing T, due to the reduction of its homogeneous decomposition. Simultaneously, the CH_4, HCl, $HSiCl_3$ and $SiCl_4$ species, which are derived from these reactions, are less and less produced in the gas phase. Below around 750°C, only MTS is detected. The slight linear decrease with T of the MTS peak area is due to thermal contraction of the gas mixture during cooling. Heterogeneous reactions (i.e., the deposition of the solid) are not expected to occur below 750°C [29].

The deposition rate was also recorded during a similar transient deposition stage, the temperature decreasing from 1020°C to 700°C with a cooling rate of -4°Cmin^{-1}. The deposition rate (R in mgmin^{-1}cm^{-2}) is reported as a function of temperature in an Arrhenius plot in Fig. 10. Several transitions in the deposition regime clearly appear while temperature is varied. The deposition rate is approximately constant from 1020 to about 950°C, suggesting a regime controlled by mass transfer (MTR). A minimum of R can be observed in an intermediate domain (~950-880°C). This singular behaviour was already observed in similar conditions [29]. It was also associated with unusual total pressure [24-25, 28] and HCl partial pressure [26, 31] dependences of R. This phenomenon was attributed to the inhibition of the deposition by HCl [26, 29], more likely through an adsorption and surface site-blocking mechanism [56]. This particular deposition regime might indeed correspond to the specific high temperature CRR sub-domain (CRR_3) mentioned by Loumagne et al. [29], as suggested by the microstructure of the reference coating described in §3-1-

2. R decreases with T at lower temperatures, showing a gradual transition from a first chemical reaction-controlled regime (CRR), with a low thermal activation at medium temperatures (880-820°C), to a second highly activated CRR regime at low temperature (T < 820°C). These two regimes are probably comparable to those already described for the CVD in steady state conditions, i.e., respectively: the intermediate temperature and low pressure CRR regime (CRR_2), associated with a control by the heterogeneous reactions (principally the chemisorption of $SiCl_3$ and CH_3 radicals) and the low temperature CRR regime (CRR_1), due to a limitation by the MTS decomposition [29-32].

The coating obtained during a decrease of the temperature exhibits a chemical composition and structure gradient. The RMS analyses (not shown) indicate that it is stoichiometric at the beginning of deposition (at high temperature) and that it contains increasing amounts of amorphous silicon near the surface (for lower deposition temperature), while the SiC grain size decreases. The AES depth profile recorded from the outer surface of the coating (see Fig 11) confirms the presence of excess silicon outwards.

3-2-2 Transient deposition by a decrease of Q_{MTS}

During the transient deposition by a decrease of the MTS flow rate, the temperature, total pressure and H_2 flow are kept constant at their standard values (T = 1000°C, P = 5 kPa, Q_{H2} = 150 sccm). Time-resolved FTIR analyses were first carried out during an immediate change of Q_{MTS}, from 0 to 50 sccm, and from 50 to 0 sccm. In both cases, steady state concentrations in the gas phase were established after less than 90 seconds.

In a second step, two symmetrical linear slopes of Q_{MTS} (each one of a length of 60 minutes), separated by a 10 minute dwell, were imposed: from Q_{MTS} = 0 to 50 sccm (0.8 $sccmmin^{-1}$) and from Q_{MTS} = 50 to 0 sccm (-0.8 $sccmmin^{-1}$), α varying from ∞ to 3 and from 3 to ∞. The gas species detected are the same as those observed for α = 3 or α = 20 in the steady state regime. As expected, symmetrical peak area profiles are observed (see Fig. 12), except at the end of the second slope, due to the difficult control of the MTS flow rate for low and decreasing values. The concavity of the peak area curves versus time is an indicator of the MTS decomposition rate and the formation of its derived species. The MTS curve is linear (in agreement with the Q_{MTS} imposed), revealing that its decomposition rate is only little influenced by the dilution in hydrogen. It is however slightly convex, the decrease of the total flow rate (the increase of the residence time) promoting the MTS decomposition. The curves are notably more convex (bell-shaped) in the case of $HSiCl_3$, CH_4 and HCl. Such a shape reveals that the formation of the hydrogenated species (in contrast to $SiCl_4$) is

enhanced by the high dilution of MTS in H_2 (at high α values). Faster slopes of Q_{MTS} (± 5 sccmmin^{-1} and ± 17 sccmmin^{-1}) were also applied in similar conditions. They were found to have no influence on the peak area profiles, i.e. no significant effect on the homogeneous reactions in the gas phase.

The deposition rate was recorded versus time during a similar linear slope of Q_{MTS} (from 50 to 0 sccm in 1h, i.e. at a rate of -0.8 sccmmin^{-1}, α varying from 3 to ∞, see Fig. 13). R decreases continuously versus time, while Q_{MTS} decreases linearly and α increases to ∞. Such a decrease of R is not due to the minor reduction of the total flow rate but rather to the dilution of the precursor. The kinetic data and the properties of the coating suggest that the standard condition (T = 1000°C, P = 5 kPa and $\alpha = 3$) belongs to a CRR_3 regime limited by the adsorption of HCl. In this case, the same regime is still expected to be obeyed as α increases (the increase of α was indeed reported to extend the CRR_3 domain [29]). The increase of the H_2 ratio will not only reduce the concentration of the effective precursors near the substrate, but it will also promote the formation of HCl, further inhibiting deposition as observed experimentally. It is worthy of note that for $P_{MTS} < 0.5$ kPa ($\alpha > 10$), lnR varies proportionally with $\ln P_{MTS}$, leading to an apparent reaction order of about $n_{MTS} = 1$.

As for the coatings prepared in steady-state conditions, the RMS spectra (not shown) recorded from the surface (i.e., corresponding to the highest α values achieved at the end of the coating) show a reduction of the SiC crystalline state. The RMS and AES depth profiles (not shown) do not reveal, however, the presence of any other phase than nanocrystalline SiC.

3-2-3 Transient deposition by a decrease of Q_{H2}

The transient deposition by a decrease of the H_2 flow was achieved with a temperature, pressure and MTS flow rate condition of 1000°C, 5 kPa and 50 sccm, respectively. During the experiment, two symmetrical slopes of Q_{H2} of 1h duration were followed, from 0 to 150 sccm and from 150 to 0 sccm , i.e. at a rate of ± 2.5 sccmmin^{-1} (α varying from 0 to 3 and from 3 back to 0).

Similarly as for the steady state deposition study, for $\alpha = 0$ (see §3-1-1), hydrocarbons such as C_2H_4, C_2H_2 and C_6H_6 were detected for $\alpha < 2$. The peak area profiles, shown in Fig. 14a-b, are symmetrical, revealing again that the concentration of MTS and the species derived from its decomposition, all increase with the MTS concentration in the initial gas mixture. The bell shape of the $SiCl_4$ profile indicates that its formation is enhanced for the lowest values of α. The hydrocarbons appear in the gas phase due (i) to the increase of the MTS partial pressure, promoting its dissociation (and hence, the formation of CH_3), and (ii) to the decrease of P_{H2}, favouring the formation of reactive unsaturated species and hence the deposition of carbon in the coating. The

three different hydrocarbons detected do not appear simultaneously during the decrease of Q_{H2} : C_2H_4 is produced first, followed by C_2H_2 and finally C_2H_6. This result is consistent with the chemical mechanism proposed to describe the maturation process of the hydrocarbons derived from C_3H_8 [57-58]. In the present case, the CH_3 radical derived from the dissociation of MTS, is recombined into C_2H_6 and undergoes a succession of dehydrogenation reactions such as (species detected by FTIR spectroscopy are in italic):

$$CH_3 \rightarrow C_2H_6 \rightarrow C_2H_5 \rightarrow \textit{C}_2\textit{H}_4 \quad (7)$$

$$C_2H_4 \rightarrow C_2H_3 \rightarrow \textit{C}_2\textit{H}_2 \quad (8)$$

$$C_2H_4 \rightarrow C_4H_6 \rightarrow C_4H_5 \rightarrow \textit{C}_6\textit{H}_6 \quad (9)$$

The maturation can even go further, leading to heavier and more reactive species such as polycyclic aromatic hydrocarbons (not detected by FTIR spectroscopy) [57-58]. The formation of these reactive species and the decrease of the concentration of C_2H_4 and C_6H_6 observed during the steady state regime for $\alpha = 0$ (as seen in Fig. 5b), suggest an increase of the carbon content in the coating for the lowest values of Q_{H2} and α (see Fig. 6, for P = 5 kPa, T = 1010°C and $\alpha < 0.5$). As in section 3-2-2, faster changes of the flow rate ($\pm$15 sccmmin^{-1} and $\pm$50 sccmmin^{-1}) were found to have no significant influence on the shape of the peak area curves, i.e. on the homogeneous reactions in the gas phase.

The deposition rate was recorded during a linear decrease of Q_{H2} versus time, from 150 to 0 sccm at a rate of -2.5 sccmmin^{-1}, for T = 985°C, P = 5 kPa and Q_{MTS} = 50 sccm (α decreasing linearly from 3 to 0) (see Fig. 15). R varies only slightly from $\alpha = 3$ to 1.8, with a minimum located at about $\alpha = 2$. Conversely, it strongly increases from $\alpha = 1.8$, to reach a maximum at about $\alpha = 0.3$, before finally slightly decreasing for the lowest values of α ($0.3 < \alpha < 0$). The variation of R with Q_{H2} can be associated with the changes in the unsaturated hydrocarbons peak areas. The increase of the heterogeneous kinetics is apparently related to the formation of these highly reactive species in the gas phase. This phenomenon is expected to lead to a carbon enrichment of the coating. Moreover, the decrease of the Q_{H2} leads to a reduction of the HCl concentration in the gas phase (see section 3-1). Lower amounts of inhibiting chlorine species are therefore adsorbed on the substrate, which could explain the increase of the deposition rate while α decreases from 1.8 to 0.3, as observed in Fig. 15.

The thickness of the transient coating (φ_{Tr}) resulting from a single decreasing slope of Q_{H2} of -2.5 sccmmin^{-1} (from 150 to 0 sccm in 1h, for T = 1010°C, P = 5 kPa, Q_{MTS}= 50 sccm) is in the range of

1-1.5 μm (see the AES depth profile in Fig 16). In agreement with the FTIR analyses, the chemical and structural analyses clearly show that the part of the coating corresponding to the lowest α values contains a large amount of free carbon. As α decreases from α = 3, the RMS analysis through the cross section of this coating indicates a gradual structural organization of the SiC phase (a decrease of the TO and LO bandwidths), followed by the appearance of increasing amounts of free carbon, as α approaches 0 (not shown). The atomic concentration profile (as measured by AES from the surface during Ar^+ sputtering, see Fig. 16) reveals that the carbon content increased progressively during deposition, to reach about 80 at.% at the surface.

A similar transient interphase (Q_{H2} = 150 → 0 sccm at -2.5 $sccmmin^{-1}$) was interposed between two stoichiometric layers (referred to as SiC_A and SiC_B, respectively), deposited in standard conditions (T = 1010°C, P = 5 kPa, α = 3), in order to be examined by TEM. Fig. 17 shows results in good agreement with the RMS and AES analyses. During deposition, a rapid transition in the microstructure is observed, from nanometre size SiC crystallites, with an isotropic arrangement, to sub-micrometre size, columnar and faulted grains, aligned along the growth direction (see Fig. 17a-c). This microstructure turns into a two phase SiC + C material during deposition, with a mixture of nanometer-sized SiC grains and short and distorted stacks of aromatic carbon layers (see Fig. 17d-e). The SiC grain size decreases and the proportion of aromatic carbon increases simultaneously, to form a thick carbon-rich region at the end of the transient stage, containing aromatic layers oriented parallel to the surface. A thin transition layer of columnar grains is subsequently observed in Fig. 17c, corresponding to the sudden switch of Q_{H2} from 0 to 150 sccm, which is applied to start the deposition of the SiC_B outer layer (containing nanometric SiC crystallites).

The first transition in the SiC microstructure/texture (from nanometric/equiaxed to sub-micrometric/columnar grains), while the composition remains close to the stoichiometry ($C_{Si} = C_C$ = 50 ±2 % at.), may appear surprising. It could be related to the elimination of a small amount of free silicon which would be present at the beginning of the coating for α = 3 (likely amorphous and in a too low amount to be detected by RMS). It could also result from a transition in the deposition regime from RCC_3, characterized by a nanocrystalline SiC grains, to RTM (T > 1000°C) or RCC_2/low pressure, these two regimes giving rise to columnar and submicrometric grains [30, 32]. Such a transition in the deposition regime (for instance related to the role of growth-inhibiting chlorine species, as suggested above) could explain the change of the deposition rate versus Q_{H2}, i.e. the minimum of R observed around α = 2 in Fig. 15, and the strong increase between α ≈ 1.5 and α = 0.3.

As suggested above, the co-deposition of aromatic carbon detected for the lowest α values clearly corresponds to the formation of increasing amounts of unsaturated hydrocarbons in the gas phase (see Fig. 14b). The analyses of coatings deposited in steady state conditions (see Fig. 6) reveal that free aromatic carbon would appear only for a very low level of α during the transient stage deposition, i.e. when a slight decrease of R is observed (see Fig. 15). This phenomenon is not understood yet. It is probably related to a change in the heterogeneous mechanism due to a different nature of the deposited solid (the free carbon phase hindering the SiC growth).

TEM specimens were prepared in similar conditions but with a faster Q_{H2}-decreasing slope (-15 $sccmmin^{-1}$ instead of -2.5 $sccmmin^{-1}$). Very similar changes are observed in the microstructure along the thickness of the transient coating. Fig. 18 shows a transient zone with steeper gradients and thinner transition layers. A thin layer of anisotropic aromatic carbon is also observed between two columnar/submicrometre grains regions (see Fig. 18b-c). In this case, the carbon layer is apparently too thin to form a continuous film, as it does not hinder the columnar growth of the grains (see the SiC_{111}-dark field image, Fig. 18c).

3-3 Adhesion of the SiC/φ_{Tr}/SiC bilayers

The model materials prepared for this study were plane SiC bilayers deposited on a silicon wafer and separated by an interphase (φ_{Tr}) resulting from a transient deposition stage. The two stoichiometric layers were synthesized in the standard conditions (P = 5kPa, T = 1000°C, α = 3 and Q_{total} = 200 sccm). The first layer (SiC_A) has a thickness of approximately 2.5 μm and the second outer layer (SiC_B) is about 0.5 μm thick. The total thickness of the SiC coating ($e_{SiCA}+e_{SiCB}$ = 3 μm) was adapted to the maximum deposition length achievable without any interruption (about 6 h), in order to avoid unwanted transient stages. The thickness ratio e_{SiCA}/e_{SiCB} was chosen sufficiently high, to minimize the contribution of the more compliant Si substrate ($E_{SiC}/E_{Si} \approx 3$), and low enough to guarantee the homogeneity of SiC_B.

The main difficulty in the assessment of the adhesion lies in the fact that the interface tested separates two layers of similar features. For this reason, 4-point flexural tests of notched beams and tensile tests of microcomposites (a single fibre coated successively with a layer of interphase and matrix) have been discarded [59-60]. Indentation-based techniques were not selected either because the micromechanical models assume well-defined damaging scenarios [61-63] which are often difficult to confirm experimentally. Instead, a local and progressive compressive/shear solicitation was directly applied with an indenter scratching the outer surface of the specimen, to reproducibly

initiate the interfacial debonding [64-68]. In the specific case of a hard coating on a hard substrate, only brittle failure modes are observed. The effect of the tangential loading is to promote tensile stress and cracking, at the trailing edge of the indenter, crack deviation to the interface and, finally, coating spallation or chipping [64-68]. The adhesion of the two SiC layers was qualitatively assessed from P_c, the load beyond which delamination occurred, when it effectively took place. This process is generally accompanied by an increase of the AE signal [64, 68]. Except for φ_{Tr}, the characteristics of the bilayer coating (SiC thicknesses, Young's modulus, surface roughness...) were assumed equivalent for all specimens.

Before testing the bilayer specimens, a scratch test experiment was carried out on a reference material consisting of a 3 μm-thick single layer of SiC ($Si/C_{at.} \approx 1$) deposited on a silicon substrate. The aim was to evaluate the damage caused by the tip on a continuously grown layer, well adherent to the Si substrate. The load/displacement and AE/displacement curves are shown in Fig. 19a. The AE signal remains stable and at low levels up to 18 N, and increases dramatically at about 19 N. A SEM analysis of the scratched specimen shows a typical pattern of parallel and arc-shaped microcracks with a regular spacing (see Fig. 19b). These cracks appear behind the indenter, due to the tensile loading caused by the frictional force [64-67]. The crack spacing gradually decreases when the load increases and the catastrophic failure of the Si substrate eventually occurs for the highest load levels (≈19 N), associated with the strong increase of the AE signal (as shown in Fig.19a). No delamination and/or chipping of the SiC coating are detected until the failure of the substrate.

3-3-1 Silicon-rich interphases

The scratch tests were carried out on two types of bilayers, the interphase (φ_{Tr}) between the layers being prepared according to two distinct transient stages (Table 1). The first one was obtained by a relatively rapid switch (in about 300 s) of P, T and α from their standard values to respectively: P = 10kPa, T = 940°C and $\alpha = 10$ (Q_{total} = 550 sccm), by maintaining these steady conditions during approximately one hour, and finally by switching back to the initial standard values to deposit the outer SiC_B layer. The objective was to insert a homogeneous interphase containing a high amount of crystallized free silicon between the SiC_A and SiC_B layers (see Fig. 6, 7b and Table 1). The second interphase was prepared by a linear decrease of the temperature from about 1000°C to 740°C (with a cooling rate of $-5°C min^{-1}$), followed by a rapid reheating up to 1000°C to start the deposition of the SiC_B layer (all the other parameters remaining unchanged: P = 5kPa, $\alpha = 3$, Q_{total} = 200 sccm).

As expected from § 3-2-1 (see also Fig. 11), the interphase material is stoichiometric at the beginning of deposition (i.e. at high temperature) and contains increasing amounts of amorphous free silicon at the end, i.e. at low temperature ($Si/C_{at.} \approx 1.2$ at $T \approx 740°C$, as deduced from AES analysis, see Table 1).

The scratch behaviour of these two specimens was very similar with that of the reference SiC single layer. The presence of these two Si-rich interphases, did not apparently affect the adhesion of the bilayers during the scratch tests: delamination or chipping of the outer coating was not observed in this case.

3-3-2 Carbon-rich interphases

Several types of carbon-rich interphases were also characterized by scratch testing (Table 1). In this case, φ_{Tr} was prepared according transient stages involving successively, at the end of the SiC_A layer deposition, (i) a decrease of Q_{H2} (or α), achieved in various well-defined conditions (specified below) and (ii) a steep increase up to the original level ($\alpha = 3$), to start the deposition of the outer SiC_B layer. The first step (i) itself, involved either (i_1) a steep drop of Q_{H2} (or α) to a constant value, followed by a dwell at the same level for a given time t, or (i_2) a linear decrease of Q_{H2} (or α) versus time down to 0, during a certain time t (Table 1, see § 3-2-3). The objective was to evaluate the influence of the composition ($Si/C_{at.}$) and the thickness (e) of the interphase on the adhesion between the two SiC layers.

$SiC_A/\varphi_{Tr}/SiC_B$ bilayers were first prepared according to i_1-type transitions with an abrupt changes of α to constant values ranging from 0 to 0.5 (Q_{H2} ranging from 0 to 50 sccm, with Q_{MTS} = 100 sccm) and for different durations (t ranging from 90 to 450 s). The carbon concentration of the interphase increases when α decreases (see Fig. 6, § 3-1-2), while e increases with t (Table 1). These specimens were submitted to TEM analyses before being subjected to scratch testing. An example of thick and carbon-rich interphase ($\alpha = 0$, t= 450 s) is shown in Figure 20. The resulting φ_{Tr} consists, successively, of a thin ($\approx$ 50 nm) and highly crystalline SiC interlayer (see the bright field (BF) and SiC_{111}-dark field (DF) images in Fig. 20b-c, respectively), followed by a thick ($\approx$ 350 nm) and anisotropic carbon-rich phase (see a the C_{002}-DF view of φ_{Tr} in Fig. 20d and a high-resolution (HR) detail of the SiC_A/φ_{Tr} transition in Fig. 20e). Although it contains silicon, the microtexture of this layer is laminar and columnar (see Fig. 20d) due to the preferential orientation of the aromatic carbon layers parallel to the surface (see Fig. 20e-f). The structural transition at the subsequent

interface is relatively steep, from carbon-rich laminar (φ_{Tr}) to isotropic nanocrsytalline SiC (SiC_B outer layer) (see Fig. 20c and 20f).

For $\alpha = 0$ ($Si/C_{at.} = 0.25$) and t equal to or longer than 150 s (i.e. for thicknesses larger than 100 nm), Fig. 21a shows that the acoustic emission signal increases strongly when the load is over 10 N. The SEM analyses of the scratch (two zones submitted to slightly different loads are shown in Fig. 21b-c) clearly show that, in addition to the regular arc-shaped brittle tensile cracks, rough and hollow zones appear on both sides of the indenter path. This phenomenon occurs at a load level beyond that corresponding to the increase of the AE signal (> 10 N), suggesting the occurrence of delamination and local chipping of the outer coating [68]. The laser profilometry analyses (see a top view in Fig. 22) showed that these depressions are actually flat and have a depth equal to the outer SiC_B layer (see Fig. 22c). Finally, AES analyses evidenced that these zones were carbon rich (~60 at.% of free carbon), confirming that this type of interphases led to the failure of the φ_{Tr}/SiC_B interface and eventually to the debonding and chipping of the outer SiC_B layer. Conversely, all the bilayers prepared with a "steep" interphase (according to an (i_1) step) and having a free carbon content lower than 60 at.% ($Si/C_{at.} > 0.25$) or a thickness under below 100 nm, were all found adherent, at least from scratch testing (Table 1).

The "gradient" interfaces prepared according to an (i_2) step (see Fig. 17 & 18, section 3-2-3) were examined in a second step. The scratch tests led to the debonding of the SiC_B outer coating provided that the thickness of the interface is equal or larger than 1500 nm (for $t \geq 3600$ s, see Fig. 17 and Table 1). A precise examination of the scratched specimen showed that delamination occurred within the interphase, close to the φ_{Tr}/SiC_B interface (i.e. at the end of phase (i_2)), i.e. for the lowest values of α and the largest amount of carbon in the coating. Thinner interphases (with sharper gradients) deposited with a faster decrease of Q_{H2} (e.g. -15 $sccmmin^{-1}$ instead of -2.5 $sccmmin^{-1}$: compare Fig. 18 with Fig. 17) were not subject to delamination when tested in similar conditions.

The occurrence of a carbon-rich region ($Si/C_{at.} \leq 0.25$) in the interphase (deposited with transient stages involving a decrease of Q_{H2} or α) is a sine qua non condition for the weakening of $SiC/\varphi_{Tr}/SiC$ bilayers interfacial properties, at least from the qualitative adhesion assessment using scratch testing. But the thickness of these regions (controlled by the duration of deposition at these low α conditions) is also a critical point for the adhesion properties. Too thin and non continuous carbon-rich interlayers do not hinder the columnar growth of all the SiC grains through φ_{Tr} (see Fig. 18). The textured polycrystalline SiC phase is not fully interrupted through these C-rich layers. A few SiC grains still anchor both SiC side regions, thus preventing the crack propagation along the C-rich layers and preserving the adhesion of the bilayers to avoid delamination. On the contrary, the

SiC grain growth is disrupted for thicker C-rich interlayers (e.g. see Fig. 17 and 20). The adhesion of the bilayers is then strongly reduced by the anisotropy of the C-rich interphase. As in in CMC, the crack deviation from SiC_A to φ_{Tr} is facilitated – and the bilayers adhesion weakened – by the poor shear strength of such lamellar structures (i.e., due to their weak Van der Waals bonds) [3].

Bilayers with a silicon-rich interphase (deposited with transient stages involving a decrease of temperature or Q_{MTS}) were all found adherent by scratch testing. The co-deposition of increasing amounts of free silicon is associated with a decrease of the SiC grain size and an isotropic texture. The TEM analyses have shown that a continuous Si interlayer totally depleted of SiC crystallites may appear at these high α levels. Yet, this interruption in the SiC grain growth has no detrimental effect on the adhesion of the bilayers. The continuity of the covalent chemical bonds and the isotropic texture are indeed both preserved through the Si-rich interphase, as well as the strong bonding between the two layers.

3-4 Connection with earlier works

This work has shown that coatings of very different nature can be deposited with a mere MTS/H_2 mixture, in well defined, but, in a few cases, unusual conditions. To our knowledge, such large ranges of α (from 0 to nearly ∞) and composition/microstructure have never been explored. These conditions are extreme, but likely to occur, if no precautions are taken, for instance during the starting up of deposition or at the end of the process. The introduction of reactive gases and their extraction by flushing (using either inert or H_2) at the end of deposition, will indeed have a strong influence on the composition of the material. Besides, certain breakdowns during steady deposition (e.g. a temperature drop, or a flow meter failure) will have similar effects. A typical case was reported by Brennan, who showed that argon flushing before the introduction of the reactant gases lead to the deposition of a carbon rich layer at the fibre/matrix interface of a SiC/SiC composite [2]. On the contrary, no carbon interfacial layer was formed when Ar was replaced by H_2. The carbon layer was attributed to the dilution of the MTS/H_2 mixture in Ar, interrupting the normal deposition of SiC. The influence of such a transition of α (from 0 to its regular value) on the gas phase and the deposit, has been clearly demonstrated in the present work.

This study has also established that, when a transient stage occurs at the beginning of deposition, or between two steady phases of SiC deposition, the resulting gradient interphase can have a strong influence on the interfacial properties. The continuous carbon layer formed at low and prolonged Q_{H2} flows is indeed detrimental to the interfacial bonding. The same situation was probably

encountered by Brennan who noticed that carbon-rich interfacial layers formed by a prior flushing in Ar resulted in weakly bonded fibre/matrix interfaces [2].

4 Conclusion

This work introduces the concept of *transient stage* in CVD. The transient deposition process consists in a gradual change of the experimental CVD parameters (temperature, initial gas composition) which leads to a change of the local composition of the gas phase and the nature (structure, composition) of the coating. When a transient stage occurs between two steady state SiC deposition cycles, an interphase (φ_{Tr}) is formed. The influence of various types of transient stages on the adhesion of the resulting SiC/φ_{Tr}/SiC bilayers was examined in details.

For transient stages resulting from a decrease of the MTS flow, an increase of the total pressure or a reduction of the temperature from the nominal conditions, the interphase obtained may contain excess silicon, in quantities depending on the α, T and P levels. The increase of the free silicon amount is accompanied by a decrease of the SiC grain size. This phenomenon can be explained by chemical changes in the homogeneous phase (MTS dissociation, formation of $SiCl_2$…), activated by temperature and pressure, as well as by the higher reactivity of the silicon containing species, as compared to hydrocarbons, for high dilutions in H_2. These silicon-rich interphases do not affect the adhesion of SiC/φ_{Tr}/SiC bilayers, at least during scratch testing.

The transient stages resulting from a decrease of the H_2 flow lead to the co-deposition of free carbon with a poor structural organization but which may cause, when deposited in high amaounts (up to 60 at.% free carbon), to an anisotropic texture. This phenomenon is related to the formation of higher amounts of reactive hydrocarbons in the gas phase (e.g. C_2H_4 and C_6H_6), in a similar manner than for the maturation process involved in the CVD of pyrocarbon from propane. The interphases with the higher carbon ratios, and having thicknesses larger than 150nm, were found particularly detrimental for the adhesion properties. Scratch tests indeed evidenced that delamination occurred at the φ_{Tr}/outer-SiC interface, leading to the local chipping of the outer SiC layer.

Acknowledgements

The authors are indebted to CNRS and Snecma for providing the grant to M.P. They greatly acknowledge J.P. Manaud from ICMCB, for his assistance in perfoming the scratch tests, as well as S. Bertrand and J. Thébault from Snecma Propulsion Solide, for valuable discussions.

References

1 G.W. Meetham, M.H. Van de Voorde, Materials for High Temperature Engineering Applications, Springer-Verlag, Berlin, Heidelberg, New York, 2000.

2 J.J. Brennan, Mater. Sci. Eng. A. 126 (1990) 203-223.

3 R. Naslain Composite Interfaces 1 (1993) 253-286.

4 T.D. Gulden, J. Am. Ceram. Soc. 51 (1968) 424-428.

5 J. Schlichting, Powd. Metal. Internat. 12 (1980) 196-200; 141-7.

6 V. Hopfe, H. Mosebach, M. Erhard, M. Meyer, J. Molec. Struct. 34 (1995) 331-342.

7 S. Jonas, W.S. Ptak, W. Sadowski, E. Walasek, C. Paluszkiewicz, J. Electrochem. Soc. 142 (1995) 2357-2362.

8 M. Ganz, N. Dorval, M. Lefebvre, M. Péalat, F. Loumagne, F. Langlais, J. Electrochem. Soc. 143 (1996) 1654-1661.

9 K. Brennfleck, S. Schneweis, R. Weiss, J. Phys. IV : JP.;9-pt 2 (1999) Pr8-1041-1048.

10 J. Heinrich, S. Hemeltjen, G. Marx, Mikrochim. Acta. 133 (2000) 209-214.

11 W.G. Zhang, K.J. Hüttinger, Chemical Vapor Deposition. 7 (2001) 173-181.

12 S.H. Mousavipour, V. Saheb, S. Ramezani, J. Phys. Chem. A. 108 (2004) 1946-1952.

13 G.S. Fischman, W.T. Petuskey, J. Am. Ceram. Soc. 68 (1985) 185-190.

14 M.D. Allendorf, C.F. Melius, J. Phys. Chem. 97 (1993) 720-728.

15 M.D. Allendorf, C.F. Melius, T.H. Osterheld, Proc. Twelfth Internat. Symp. Chem. Vapor Dep., Electrochemical Society Proceedings Series, Pennington, 93-2 (1993) 20-26.

16 GD Papasouliotis, SV Sotirchos, J. Electrochem. Soc. 141 (1994) 1599-1611.

17 Q. Zeng, K. Su, L. Zhang, Y. Xu, L. Cheng, X. Yan, J. Phys. Chem. Ref. Data. 35 (2006) 1385-1390.

18 Y Ge, MS Gordon, F Battaglia, RO Fox, J. Phys. Chem. A. 111 (2007) 1462-1474; Ibid. 1475-1486; Ibid. 114 (2010) 2384-2392.

19 G Chichignoud, M Ucar-Morais, M Pons, E Blanquet. Surf. Coat. Tech. 201 (2007) 8888-8892.

20 J. Deng, K. Su, X. Wang, Q. Zeng, L. Cheng, Y. Xu, L. Zhang, Theoretical Chemistry Accounts. 122 (2009) 1-22.

21 J. Deng, K. Su, Q. Zeng, X. Wang, L. Cheng, Y. Xu, L. Zhang, 15 (2009) 281-290.

22 E. Minford, R.E. Stevens, V.L. Magnotta, P.N. Dyer, T.R. Watkins, D.J., Mat. Res. Soc. Symp. Proc., Besmann TM, Gallois BM eds., Pittsburg, 168 (1990) 233-238.

23 A. Parretta, G. Giunta, E. Cappelli, V. Adoncecchi, V. Vittori, Ibid. 227-232.

24 T.M. Besmann, B.W. Sheldon, M.D. Kaster. Surf. Coat. Tech. 43-44 (1990)167-175.

25 F. Langlais,C. Prebende, B. Tarride, R. Naslain, J. Phys. IV Colloq. C5 Suppl. 5, 50 (1989) 93-103.

26 T.M. Besmann, B.W. Sheldon, T.S. Moss III, M.D. Kaster, J. Am. Ceram Soc. 75 (1992) 2899-2903.

27 D. Neuschutz, F. Salehomoum, Mat. Res. Soc. Symp. Proc., T.M. Besmann, B.M. Gallois, J.W. Warren eds., Pittsburg, 250 (1992) 41-46.

28 F. Loumagne, F. Langlais, R. Naslain, J. Phys. IV. 3 (1993) 527-533.

29 F. Loumagne, F. Langlais, R. Naslain, J. Cryst. Growth. 155 (1995) 198-204.

30 F. Langlais, F. Loumagne, D. Lespiaux, S. Schamm, R. Naslain, J. Phys. IV. 5 (1995) C5-105-112.

31 F. Loumagne, F. Langlais, R. Naslain, J. Cryst. Growth. 155 (1995) 205-213.

32 F. Loumagne, F. Langlais, R. Naslain, S. Schamm, D. Dorignac, J Sévely, Thin Solid Films. 254 (1995) 75-82.

33 C.Y. Tsai, S.B. Desu, C.C. Chiu, J. Mater. Res. 9 (1994) 104-111.

34 D.J. Kim, D.J. Choi, Y.W. Kim, Thin Solid Films. 266 (1995) 192-7.

35 J. Yeheskel, M.S. Dariel, J. Am. Ceram. Soc. 78 (1995) 229-232.

36 W.J. Lackey, S. Vaidyaraman, B.N. Beckloff, T.S. Moss III, J.S. Lewis, J. Mater. Res. 13 (1998) 2251-2260.

37 G.D. Papasouliotis, S.V. Sotirchos, Chem. Vap. Deposition. 4 (1998) 235-246.

38 G.D. Papasouliotis, S.V. Sotirchos, J. Mater. Res. 14 (1999) 3397-3409.

39 H.S. Kim, D.J. Choi, Thin Solid Films. 312 (1998) 195-201.

40 H.S. Kim, D.J. Choi, J. Am. Ceram. Soc. 82 (1999) 331-7.

41 Y.J. Lee, D.J. Choi, J.I.Y. Park, G.W. Hong, J. Mater. Sci. 35 (2000) 4519-4526.

42 J.H. Oh, B.J. Oh, D.J. Choi, G.H. Kim, H.S. Song, J Mater Sci. 36 (2001) 1695-1700.

43 H. Sone, T. Kaneko, N. Miyakawa, J. Cryst. Growth. 219 (2000) 245-252.

44 W.G. Zhang, K.J. Hüttinger, 7 (2001) 167-172.

45 Y. Kajikawa, S. Noda, H. Komiyama, Chem. Vap. Dep. 8 (2002) 99-104.

46 B. Reznik, D. Gerthsen, W. Zhang, K.J. Hüttinger, J. Europ. Ceram. Soc. 23 (2003) 1499-1508.

47 E. López-Honorato, P.J. Meadows, J. Tan, P. Xiao, J. Mater. Res. 23 (2008) 1785-1796.

48 Y. Yang, W. Zhang, J. Central South Univ. Tech. (English Edition). 16 (2009) 730-737.

49 C. Lu, L. Cheng, C. Zhao, L. Zhang, Y. Xu, Appl. Surf. Sci. 255 (2009) 7495-7499.

50 F. Langlais, A. Kelly, C. Zweben eds. Oxford, Elsevier Science Ltd. 4 (2000) 611-643.

51 F. Christin, Adv. Eng. Mater. 4 (2002) 903-912.

52 J. Berjonneau, F. Langlais, G. Chollon, Surf. Coat. Tech. 201 (2007) 7273-7285.

53 D.W. Feldman, J.H. Parker, W.J. Choyke, L. Patrick, Phys. Rev. 173 (1968) 787-793.

54 Y. Ward, R.J. Young, R.A. Shatwell, J. Mater. Sci. 39 (2004) 6781-6790.

55 G. Chollon, R. Naslain, C. Prentice, R. Shatwell, P. May, J. Eur. Ceram. Soc. 25 (2005) 1929-1942.

56 M.T. Schulberg, M.D. Allendorf, D.A. Outka, Surf. Sci., 341 (1995) 262-272.

57 F. Langlais, H. Le Poche, J. Lavenac, O. Feron, EUROCVD-15, Proceedings of the International Symposium, A. Devi, R. Fischer, H. Parala, M. Hitchman eds., Electrochem. Soc. Proc., 2005-09,pp. 73-86.

58 C. Descamps, G.L. Vignoles, O. Féron, F. Langlais, J. Lavenac, J. Electrochem. Soc. 148 (2001) C695-C708.

59 P.G. Charalambides, J. Lund, A.G. Evans, R.M. McMeeking, J. Appl. Mech. Trans. ASME. 56 (1989) 77-82.

60 J. Lamon, F. Rebillat, A.G. Evans, J. Am. Ceram. Soc. 78 (1995) 401-405.

61 D.B. Marshall, A.G. Evans, J. Appl. Phys. 56 (1984) 2632-2638.

62 J.B. Davis, H.C. Cao, G. Bao, A.G. Evans, Act. Met. Mater. 39 (1991) 1019-1024.

63 D. Chicot, P. Démarécaux, J. Lesage, Thin Solid Films. 283 (1996) 151-157.

64 S.J. Bull, Surf. Coat. Tech. 50 (1991) 25-32.

65 S.J. Bull, Tribol. Int. 30 (1997) 491-498.

66 J. Den Toonder, J. Malzbender, G. De With, R. Balkenende, J. Mater. Res. 17 (2002) 224-233.

67 J. Malzbender, J.M.J. Den Toonder, A.R. Balkenende, G. De With, Mater. Sci. Eng. R 36 (2002) 47-103.

68 L. Chouanine, M. Takano, F. Ashihara, O. Kamiya, J. Mater. Sci. 40 (2005) 5703-5710.

Table Caption

Table 1: CVD conditions for the synthesis of the various interphases (φ_{Tr}) ($Si/C_{at.}$ and e are respectively the atomic ratio and the thickness of φ_{Tr}).

φ_{Tr} CVD conditions				$Si/C_{at.}$	e (nm)	Debonding
α	P (kPa)	T (°C)	t (s)			
10	10	940	3600	~3	-	No
3	5	1000→740	3600	1→1.2	~250	No
0	5	1000	450	~0.25	~350	**Yes**
0.25	5	1000	300	~0.43	~300	No
0.5	5	1000	300	~0.67	~200	No
0	5	1000	150	~0.25	~100	**Yes**
0	5	1000	90	-	~30	No
3→0	5	1000	600	1→~0.25	~200	No
3→0	5	1000	3600	1→~0.25	~1500	**Yes**

Table 1: CVD conditions for the synthesis of the various interphases (φ_{Tr}) ($Si/C_{at.}$ and e are respectively the atomic ratio and the thickness of φ_{Tr}).

Figure Captions

Figure 1 : CVD reactor geometry and configuration during (a) in situ gas phase analysis and (b) measurement of the deposition rate

Figure 2 : In situ FTIR spectrum of the gas phase (P = 5 kPa, T = 1000°C, $\alpha = 3$)

Figure 3 : Peak areas of the main gas species as a function of temperature (P = 5 kPa, $\alpha = 3$)

Figure 4 : In situ FTIR spectrum of the gas phase (P = 5 kPa, T = 1000°C, $\alpha = 0$, compared with $\alpha = 3$)

Figure 5 : Peak areas of the main gas species (a) and the hydrocarbons (b) as function of temperature (P = 5 kPa, $\alpha = 0$)

Figure 6 : Si/C atomic ratio in the coating as a function of P, T and α

Figure 7 : Raman spectra of the coatings as a function of α: (a): T = 1010°C, P = 5 kPa (except*) and (b): P = 10 kPa (except °)

Figure 8 : SEM (a) and TEM images of a coating obtained in standard conditions (P = 5kPa, T = 1000°C, $\alpha = 3$). (b) : SAED pattern (with d-spacings and Miller indices for β-SiC), (c) : SiC_{111} dark field

Figure 9 : Peak areas of the main gas species as a function of time and deposition temperature (-8°Cmin^{-1}, P = 5 kPa, $\alpha = 3$)

Figure 10 : Deposition rate R as a function of time and deposition temperature (-4°Cmin^{-1}, P = 5 kPa, $\alpha = 3$)

Figure 11 : AES profile of a coating obtained by a decrease of temperature (from 1020 to 700°C at a rate of -4°Cmin^{-1}, P = 5 kPa, $\alpha = 3$)

Figure 12 : Peak areas of the main gas species as a function of time and Q_{MTS} ($\pm$0.8 sccmmin^{-1}, P = 5 kPa,T = 1000°C, Q_{H2} = 150 sccm)

Figure 13 : Deposition rate R as a function of time and Q_{MTS} (-0.8 sccmmin^{-1}, P = 5 kPa,T = 1000°C, Q_{H2} = 150 sccm)

Figure 14 : Peak areas of the main gas species (a) and the hydrocarbons (b) as a function of time and Q_{H2} ($\pm$2.5 sccmmin^{-1}, P = 5 kPa, T = 1000°C, Q_{MTS} = 50 sccm)

Figure 15 : Deposition rate R as a function of time and Q_{H2} (-2.5 sccmmin^{-1}, P = 5 kPa, T = 985°C, Q_{MTS} = 50 sccm)

Figure 16 : AES profile of a coating obtained by a decrease of Q_{H2} (from 150 to 0 sccm at a rate -2.5 sccmmin^{-1}, P=5kPa,T=1000°C, Q_{MTS}=50sccm)

Figure 17 : TEM images of a coating obtained by a linear decrease of Q_{H2} (from 150 to 0 sccm at a rate -2.5 sccmmin^{-1}, P=5kPa,T=1000°C, Q_{MTS}=50sccm). (a)-(c) : SiC_{111} dark field, (d) : C_{002} dark field, (e) : high resolution.

Figure 18: TEM images of a coating obtained by a linear decrease of Q_{H2} (from 150 to 0 sccm at a rate -15 sccmmin^{-1}, P=5kPa,T=1000°C, Q_{MTS}=50sccm). (a) bright field, (b) : C_{002} dark field, (c) SiC_{111} dark field.

Figure 19 : (a) Load-displacement curve and E.A. signal recorded during the scratch testing of a SiC monolayer (b) morphology of the scratched specimen at F = 12N (white dotted arrow shows the scratching direction).

Figure 20 : TEM images of a $SiC_A/\varphi_{Tr}/SiC_B$ bilayer obtained by a steep drop of Q_{H2} (Q_{H2} = 300→0 sccm, P = 5kPa,T = 1000°C, Q_{MTS} = 100sccm, t= 450 s). (a-b) bright field (BF) , (c) SiC_{111}-dark field (DF), (d) C_{002}-DF.

Figure 20 : TEM images of a $SiC_A/\varphi_{Tr}/SiC_B$ bilayer obtained by a steep drop of Q_{H2} (Q_{H2} = 300→0 sccm, P = 5kPa,T = 1000°C, Q_{MTS} = 100sccm, t= 450 s). (e-f) high-resolution (HR).

Figure 21 : (a) Load-displacement curve and E.A. signal recorded during the scratch testing of a bilayer with a carbon-rich interphase ($Si/C_{at.}$ = 0.25, $e_{\varphi Tr}$ = 350nm) (b-c) morphology of the scratched specimen: (b) F=11 N, (c) F = 12 N. (white dotted arrows show the scratching direction).

Figure 22 : Topography (from laser profilometry) of a scratched bilayer with a carbon-rich interphase ($Si/C_{at.}$ = 0.25, $e_{\varphi Tr}$ = 350nm) (a) Z mapping, (b) Z profile along X, (c) Z profile along Y. (white dotted arrows show the scratching direction).

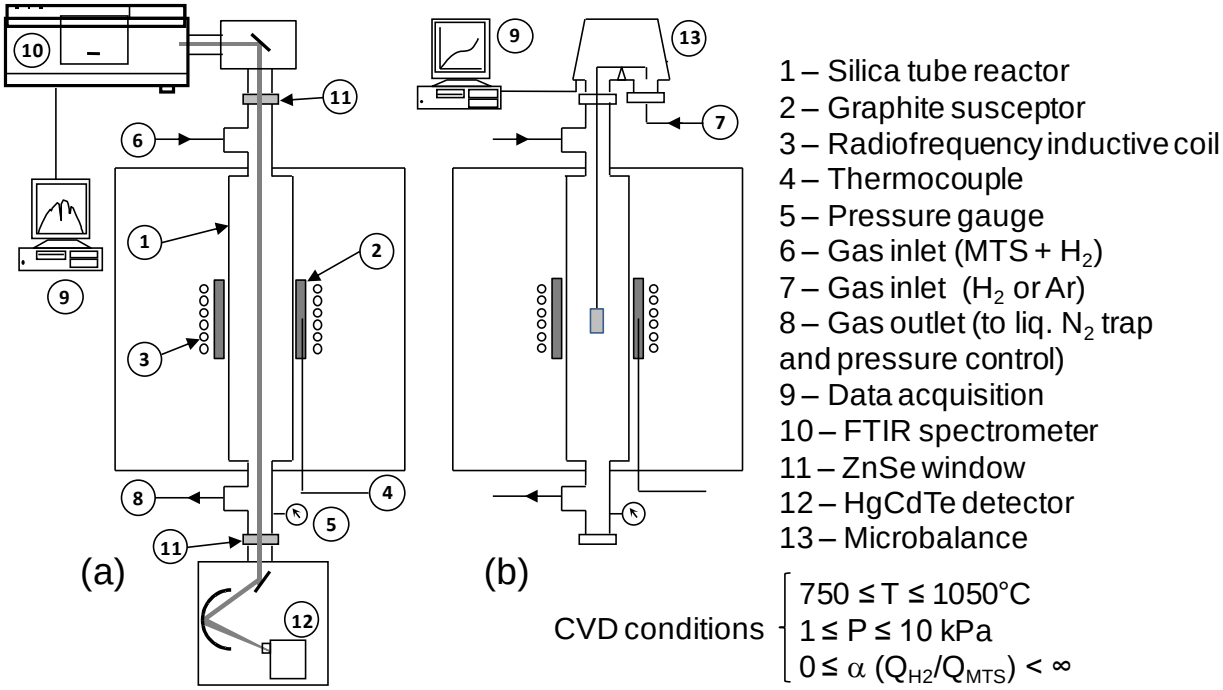

Figure 1 : CVD reactor geometry and configuration during (a) measurement of the deposition rate and (b) in situ gas phase analysis

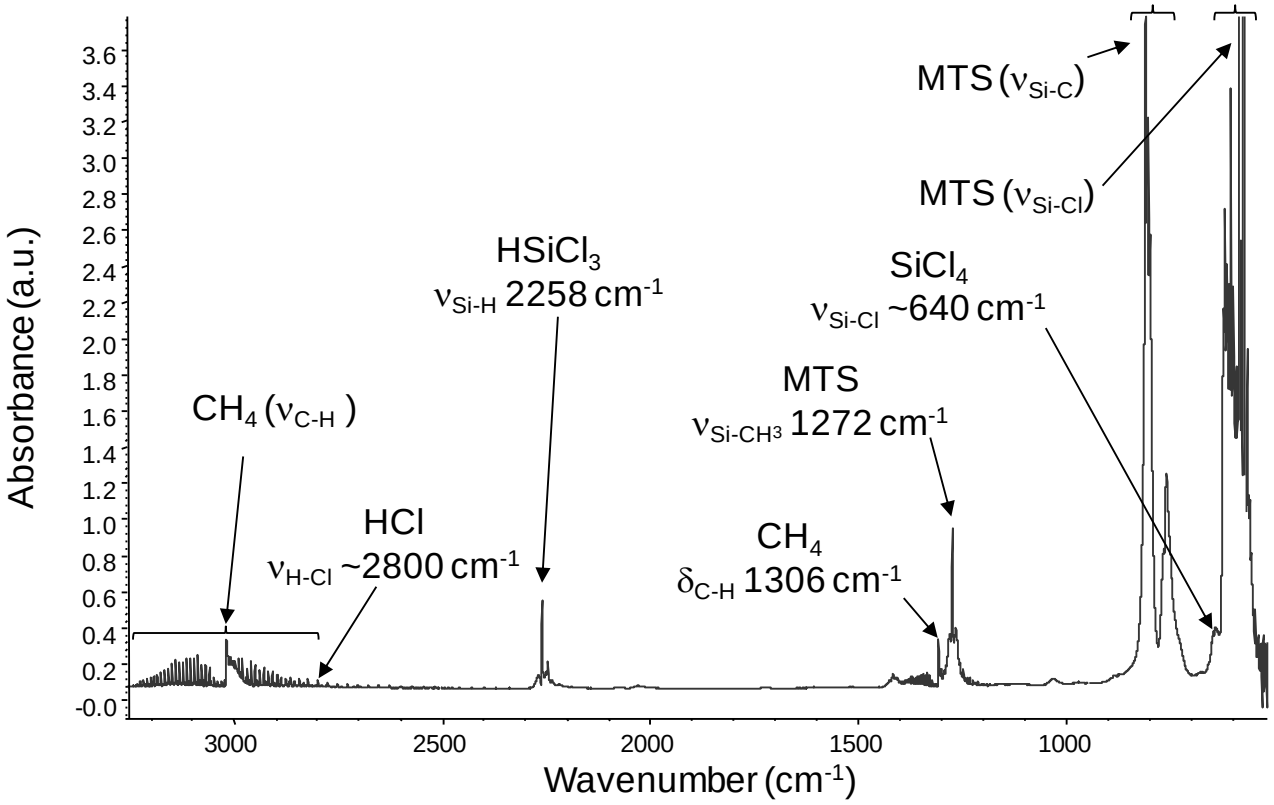

Figure 2 : In situ FTIR spectrum of the gas phase (P = 5 kPa, T = 1000°C, α = 3)

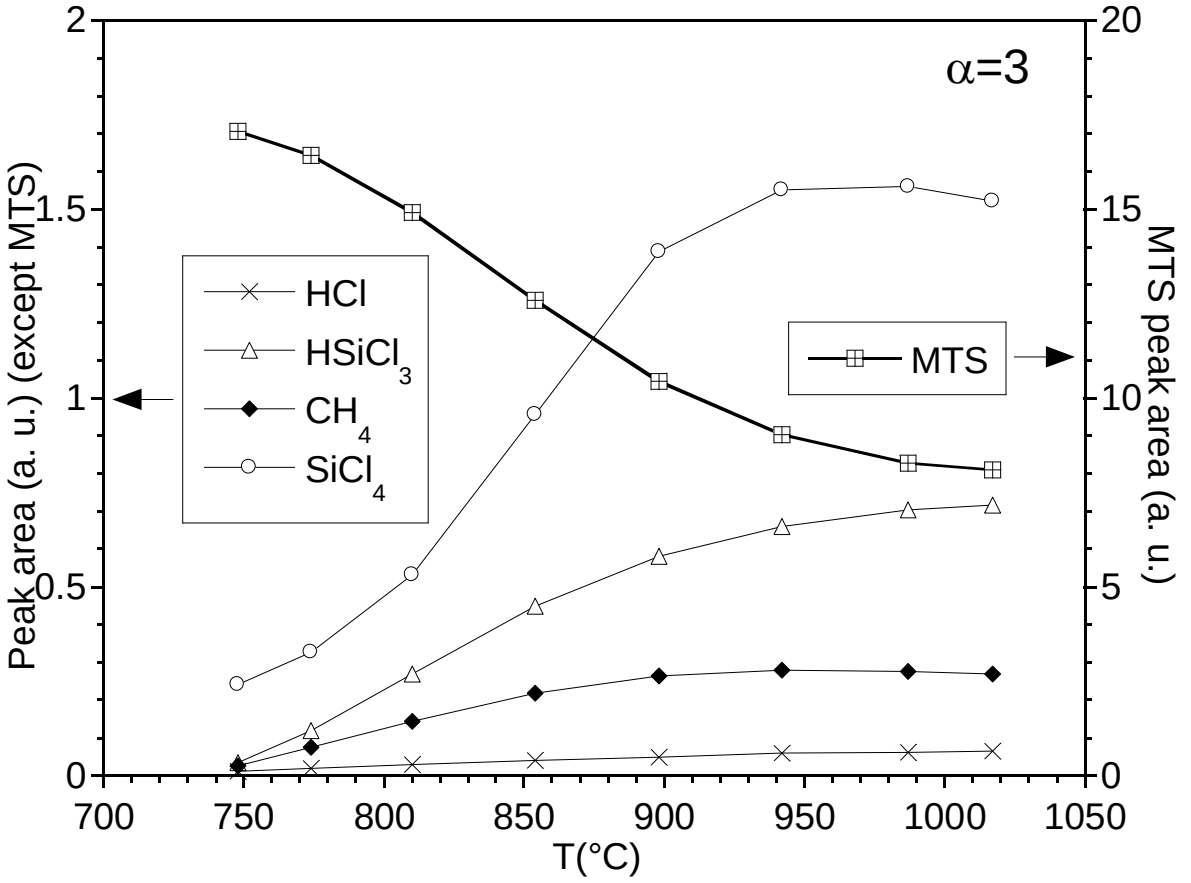

Figure 3 : Peak areas of the main gas species as a function of temperature (P = 5 kPa, α = 3)

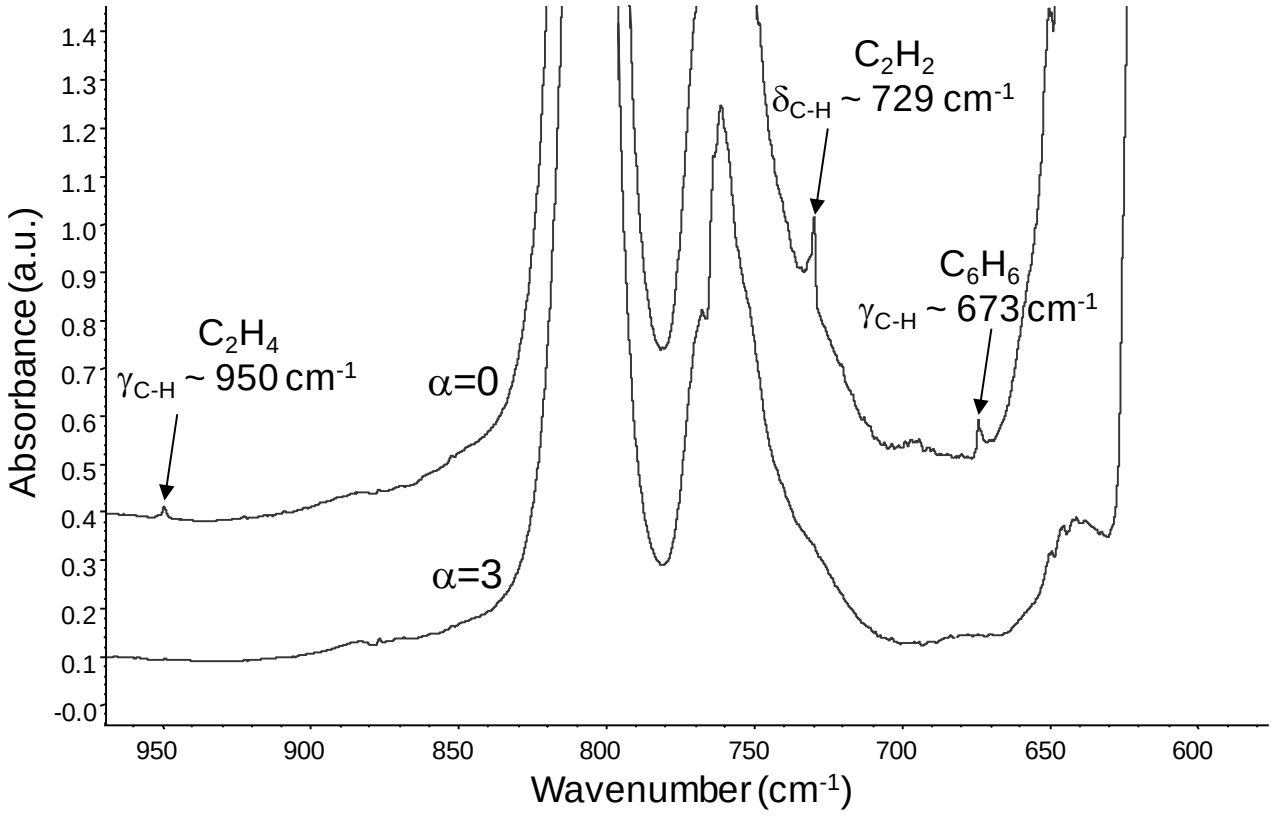

Figure 4 : In situ FTIR spectrum of the gas phase (P = 5 kPa, T = 1000°C, α = 0, compared with α = 3)

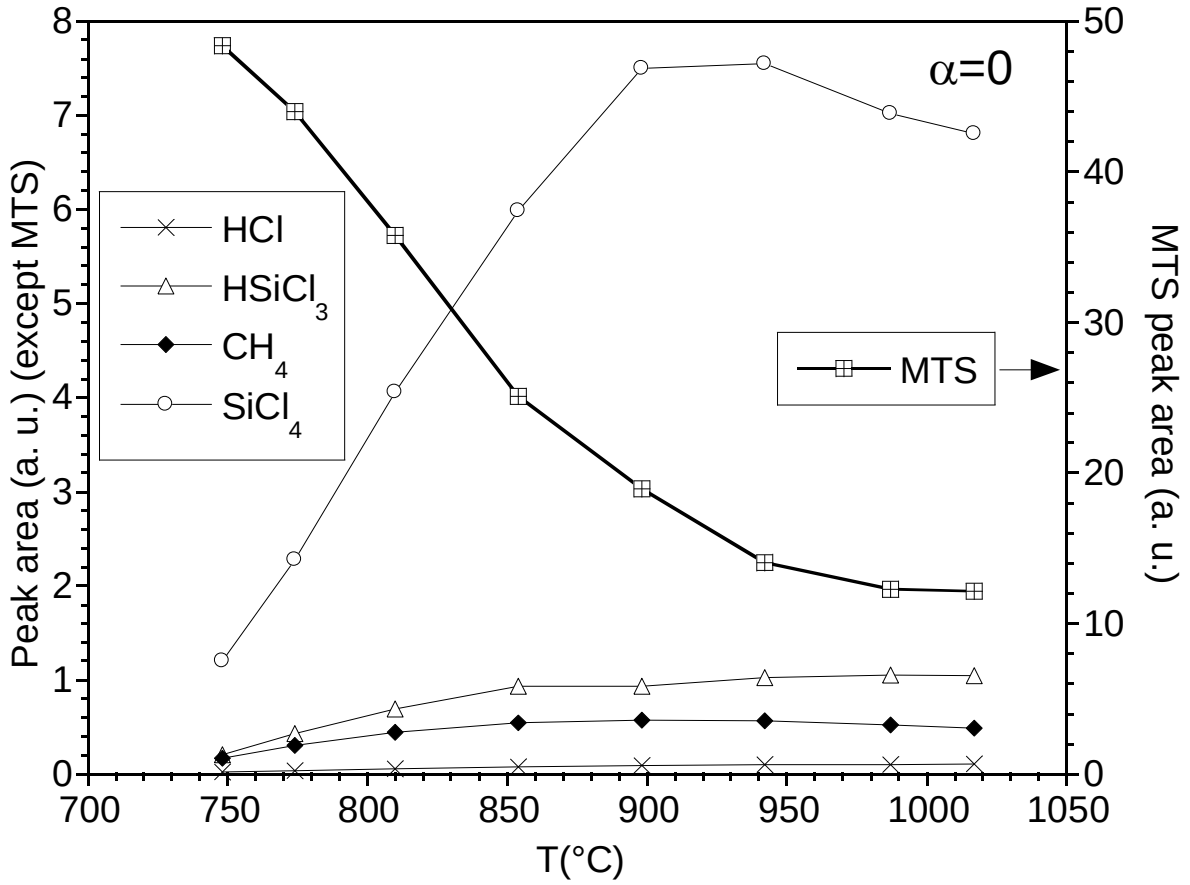

Figure 5a : Peak areas of the main gas species as function of temperature (P = 5 kPa, $\alpha = 0$)

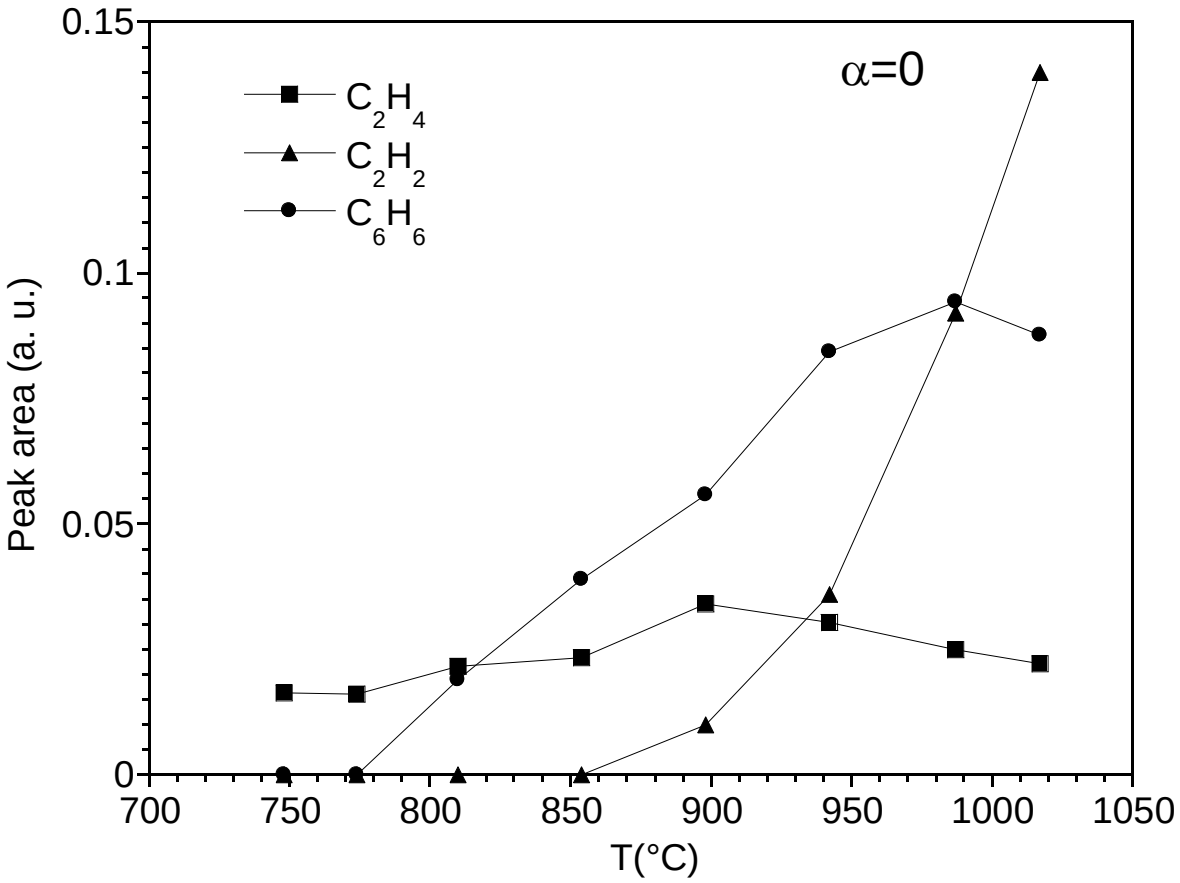

Figure 5b : Peak areas of the main gas species as a function of T (P = 5 kPa, $\alpha = 0$)

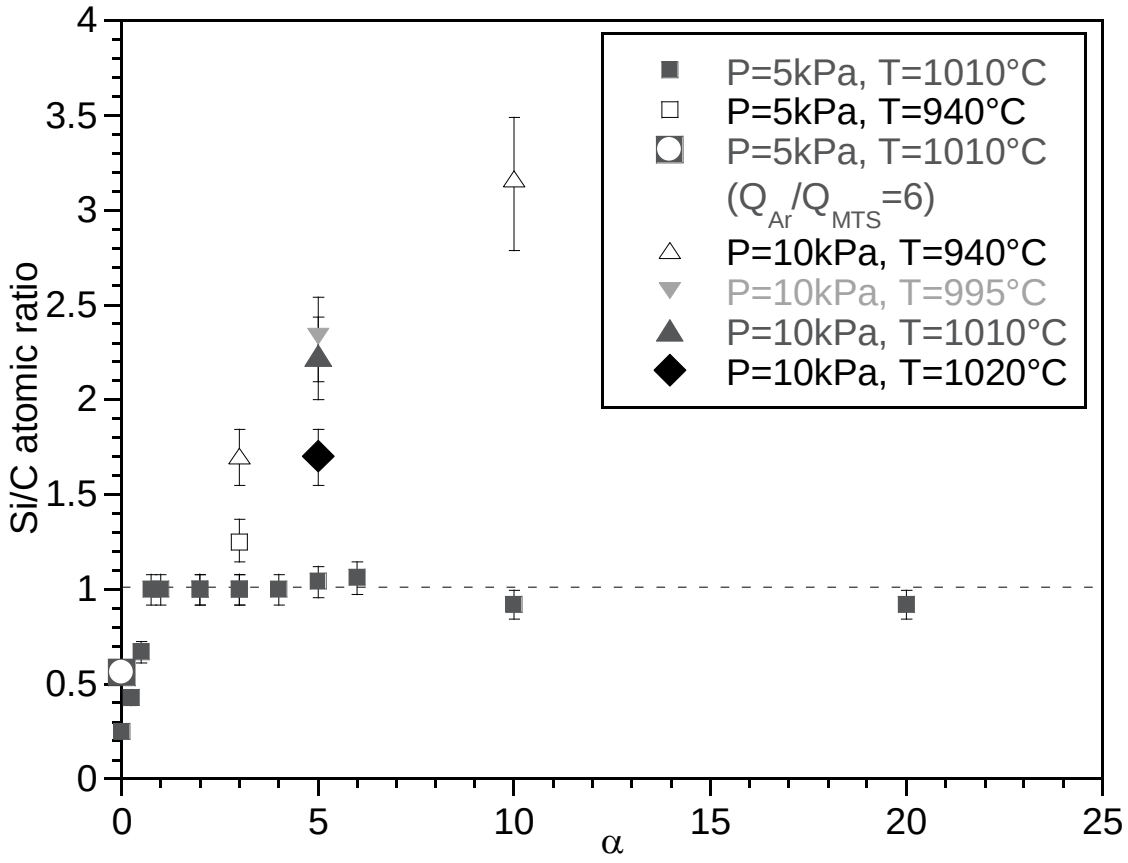

Figure 6 : Si/C atomic ratio in the coating as a function of P, T and α

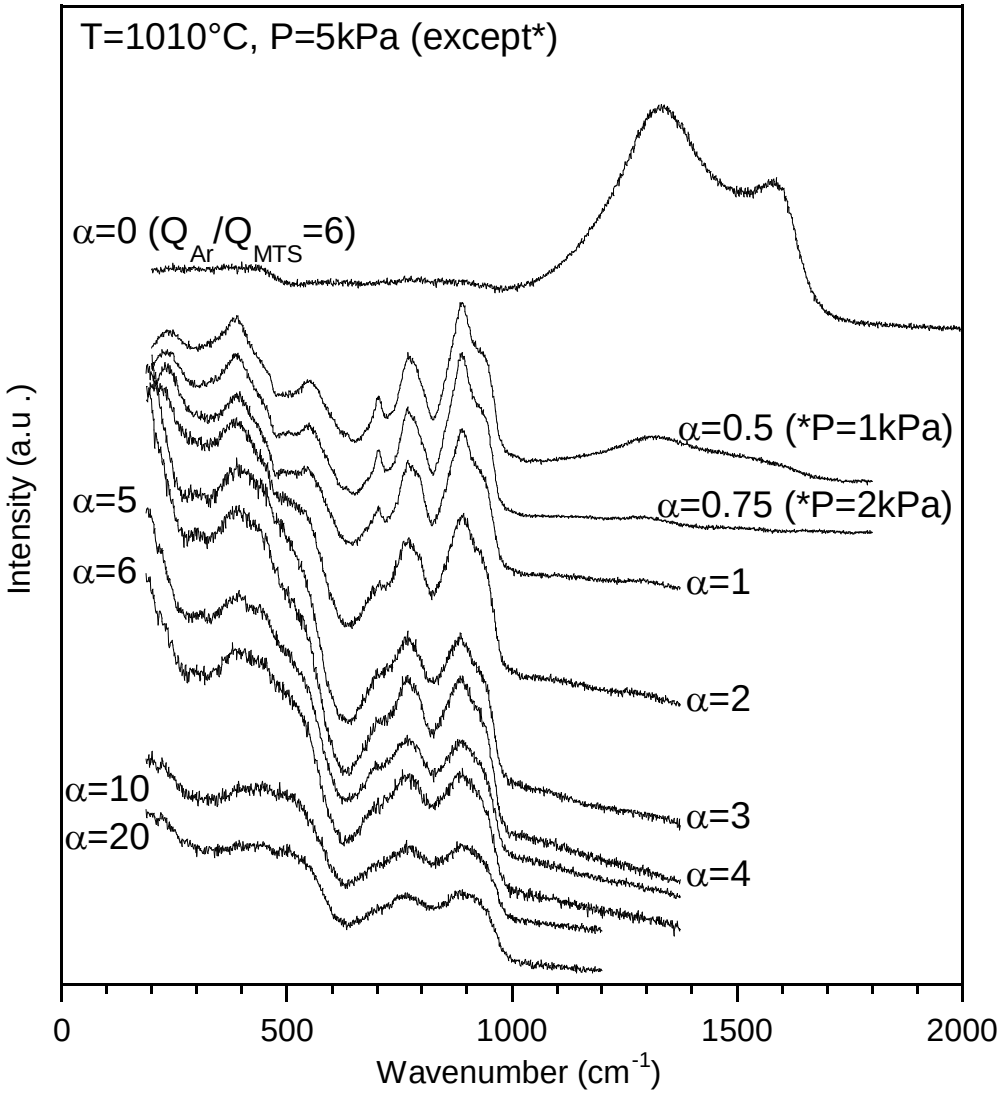

Figure 7a : Raman spectra of the coatings as a function of α (T = 1010°C, P = 5 kPa, except*)

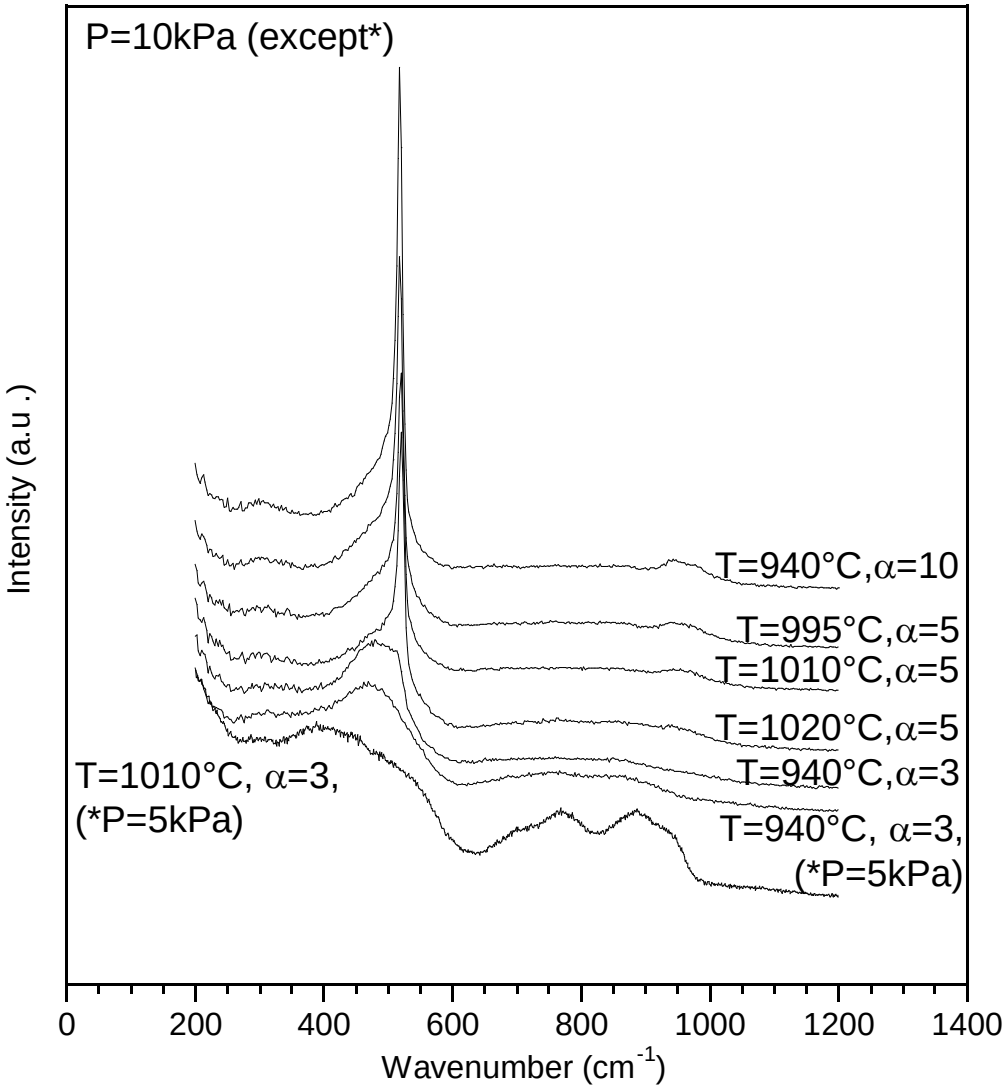

Figure 7b : Raman spectra of the coatings as a function of α (P = 10 kPa except *)

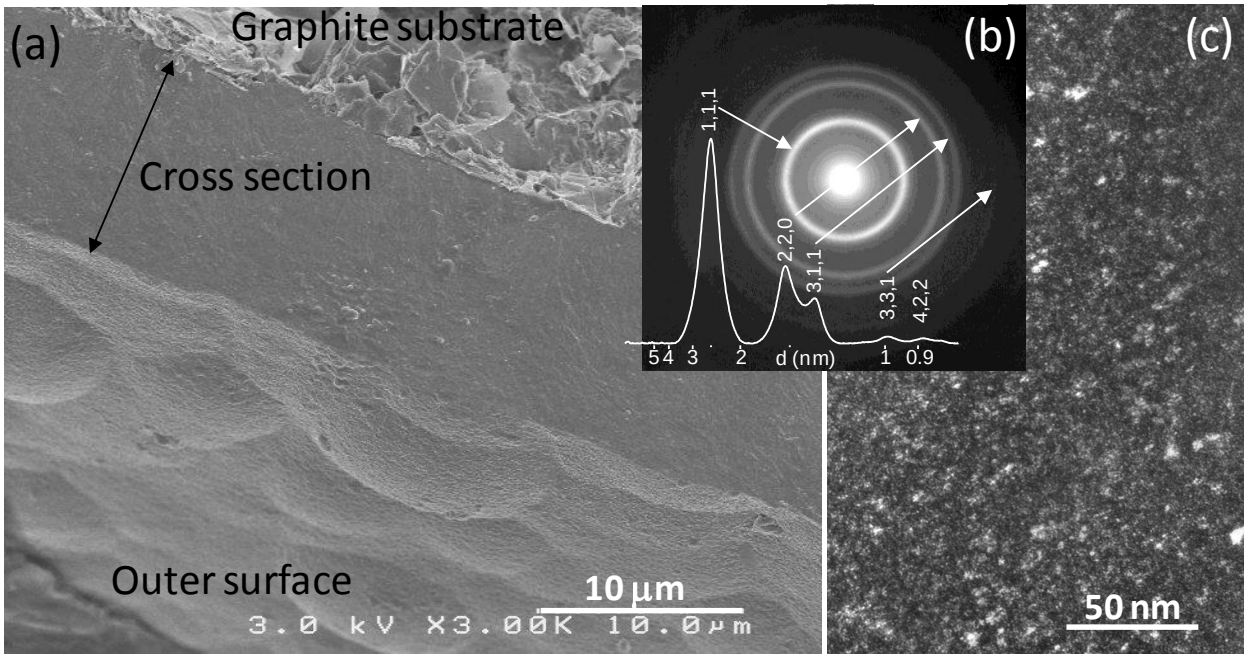

Figure 8 : SEM (a) and TEM images of a coating obtained in standard conditions (P = 5 kPa, T = 1000°C, $\alpha = 3$). (b) : SAED pattern (with d-spacings and Miller indices for β-SiC), (c) : SiC_{111} dark field

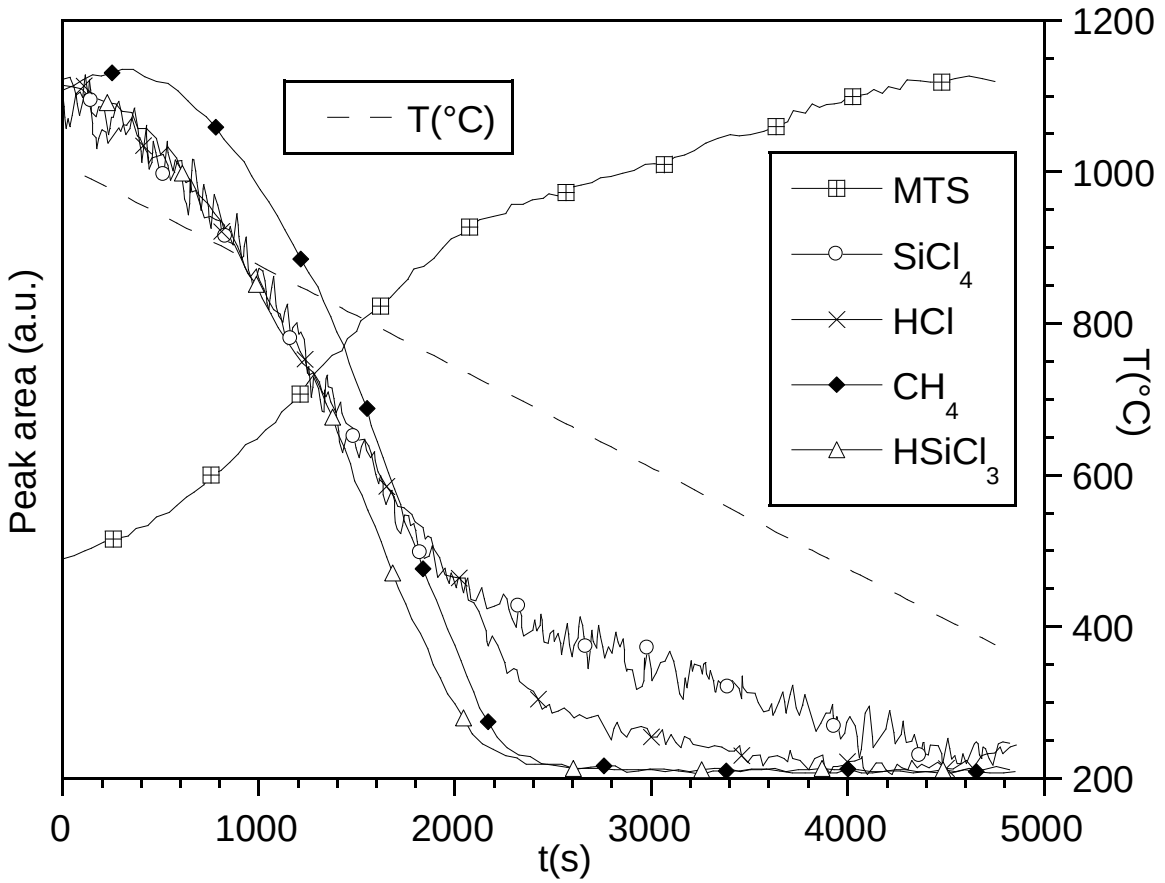

Figure 9 : Peak areas of the main gas species as a function of time and deposition temperature ($-8°C min^{-1}$, P = 5 kPa, $\alpha = 3$)

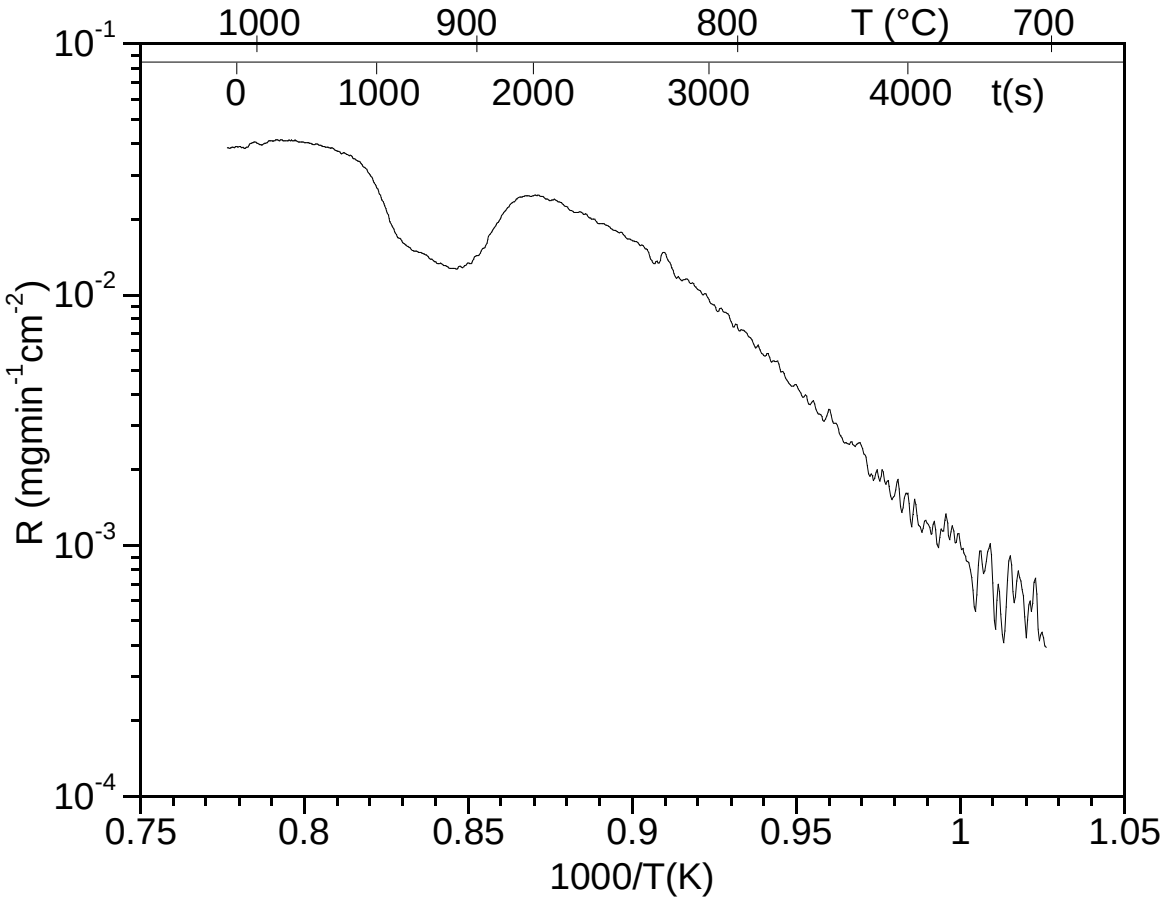

Figure 10 : Deposition rate R as a function of time and deposition temperature ($-4°Cmin^{-1}$, P = 5 kPa, $\alpha = 3$)

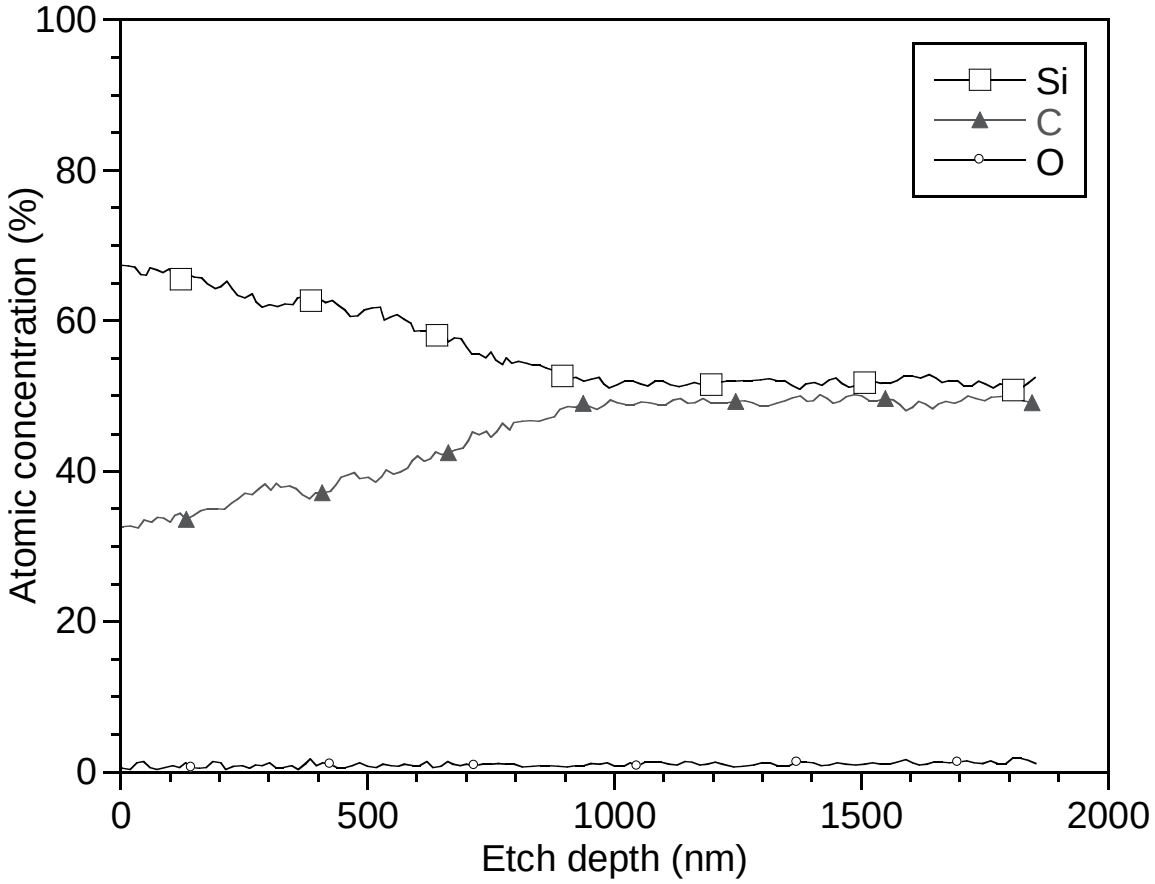

Figure 11 : AES profile of a coating obtained by a decrease of temperature (from 1020 to 700°C at a rate of -4°Cmin^{-1}, P = 5 kPa, α = 3)

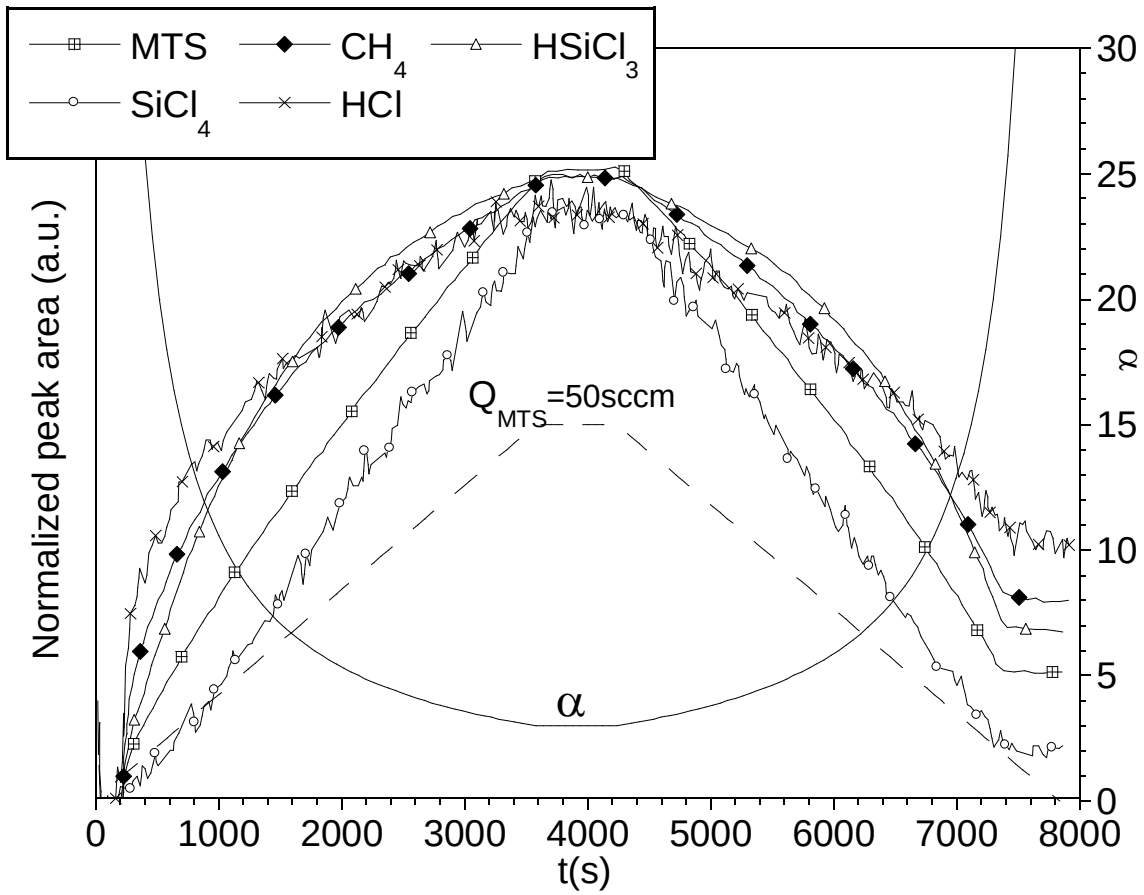

Figure 12 : Peak areas of the main gas species as a function of time and Q_{MTS} (± 0.8 sccmmin^{-1}, P = 5 kPa,T = 1000°C, Q_{H2} = 150 sccm)

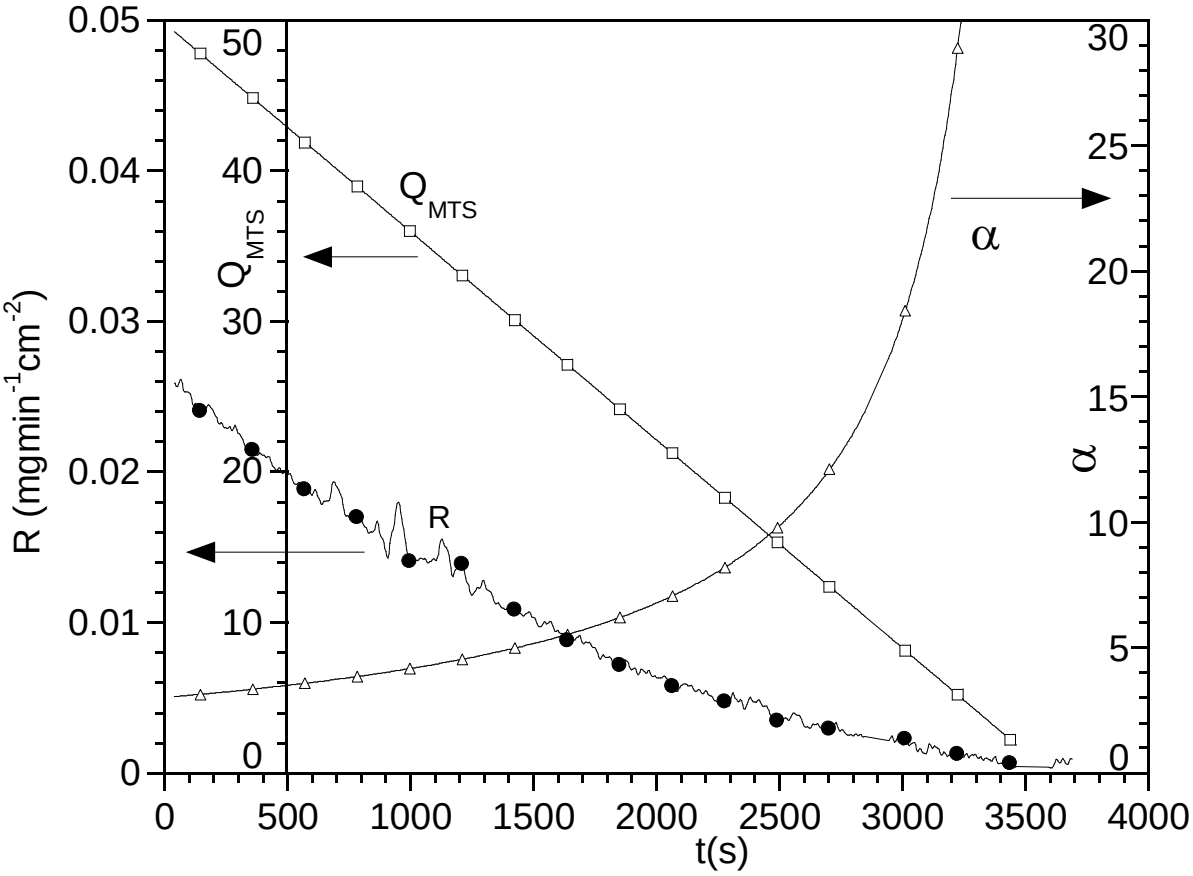

Figure 13 : Deposition rate R as a function of time and Q_{MTS} (-0.8 sccmmin^{-1}, P = 5 kPa,T = 1000°C, Q_{H2} = 150 sccm)

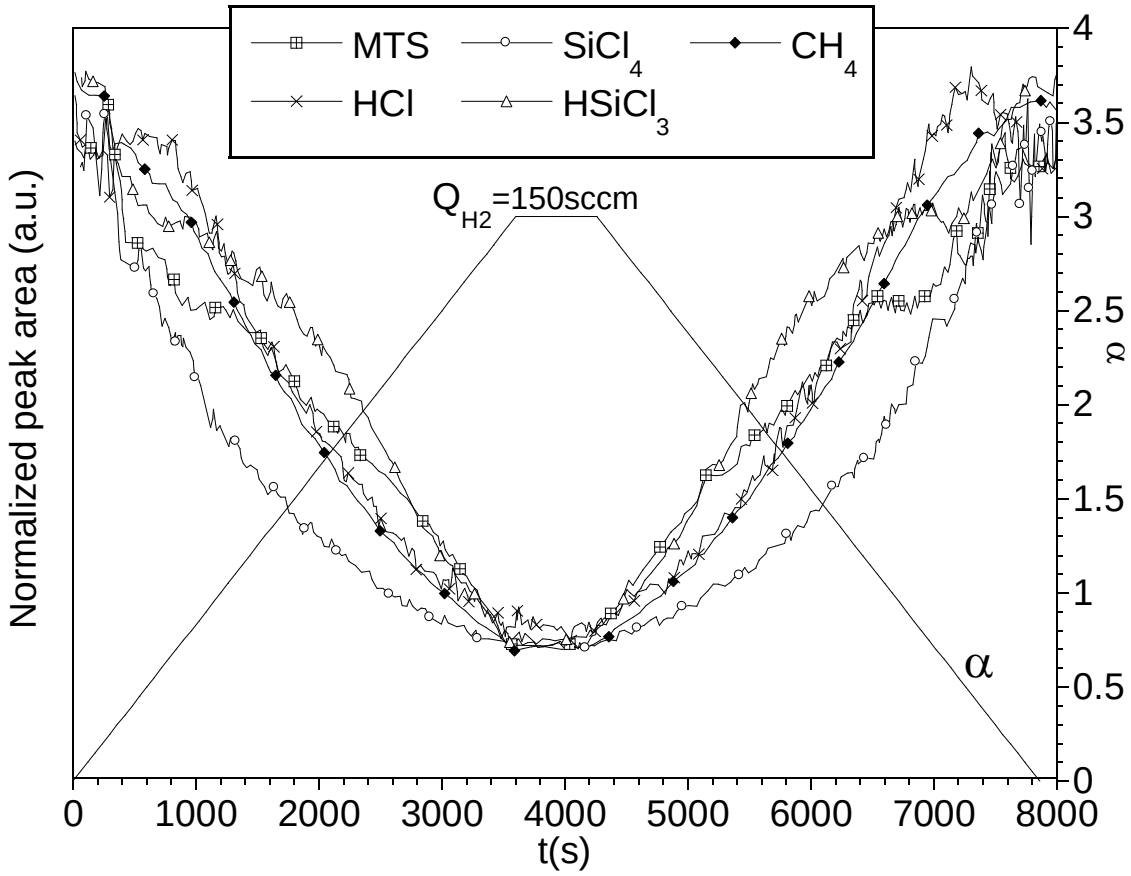

Figure 14a : Peak areas of the main gas species as a function of time and Q_{H2} (±2.5 sccmmin^{-1}, P = 5 kPa, T = 1000°C, Q_{MTS} = 50 sccm)

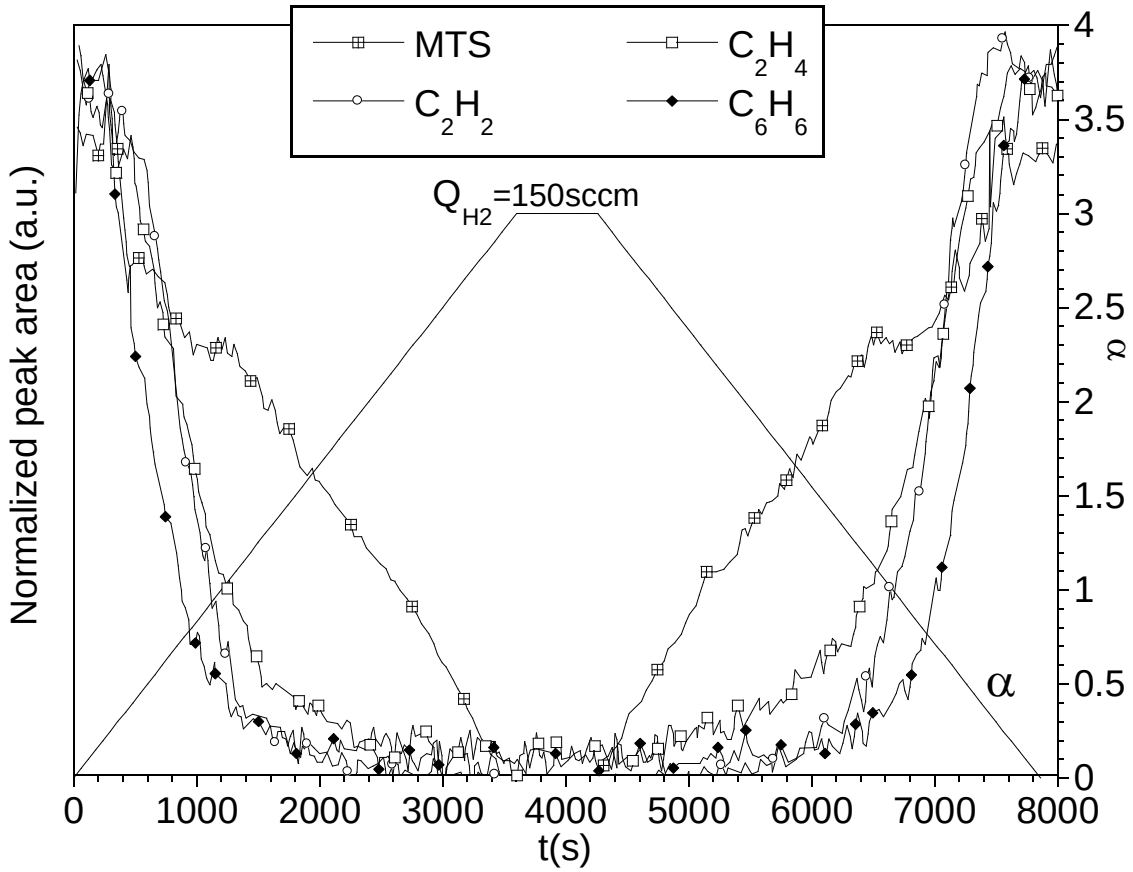

Figure 14b : Peak areas of the unsaturated hydrocarbons as a function of time and Q_{H2} (±2.5 sccmmin^{-1}, P = 5 kPa, T = 1000°C, Q_{MTS} = 50 sccm)

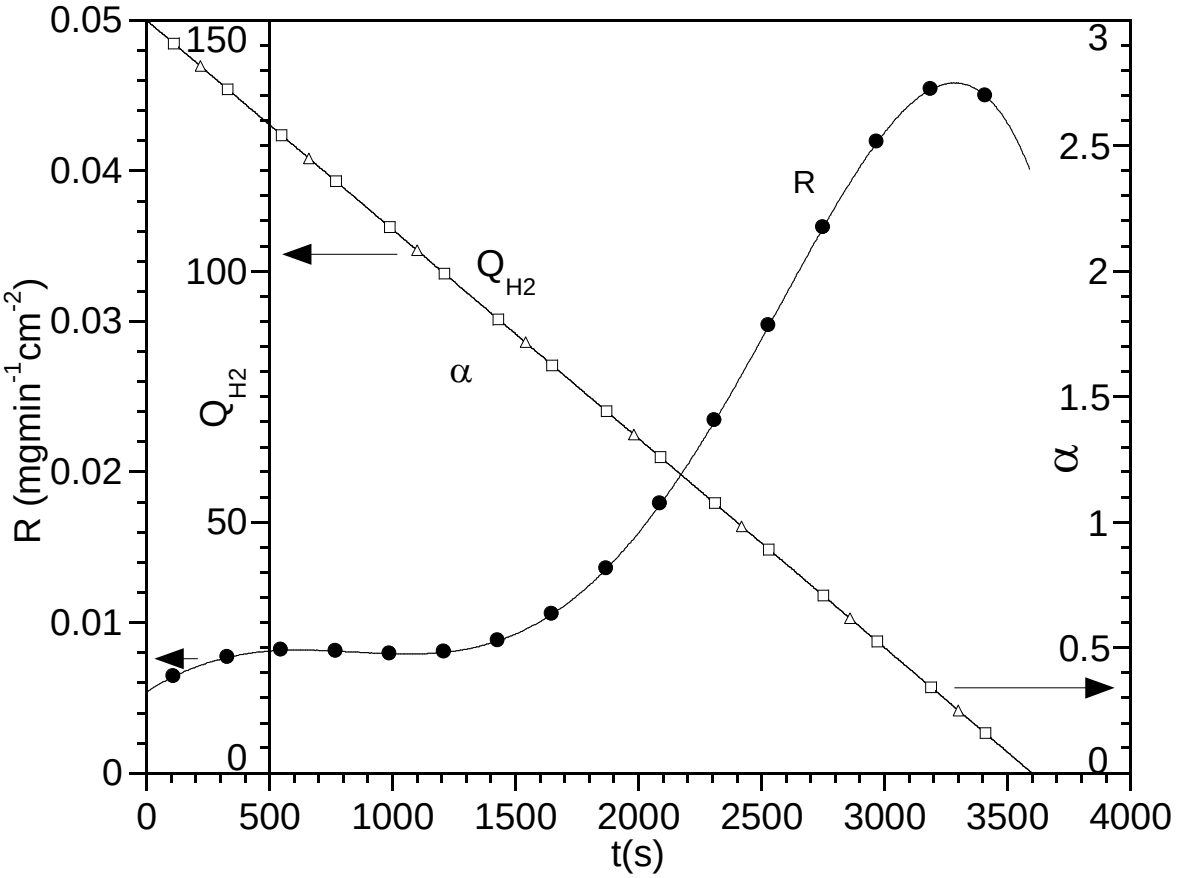

Figure 15 : Deposition rate R as a function of time and Q_{H2} (-2.5 sccmmin^{-1}, P = 5 kPa, T = 985°C, Q_{MTS} = 50 sccm)

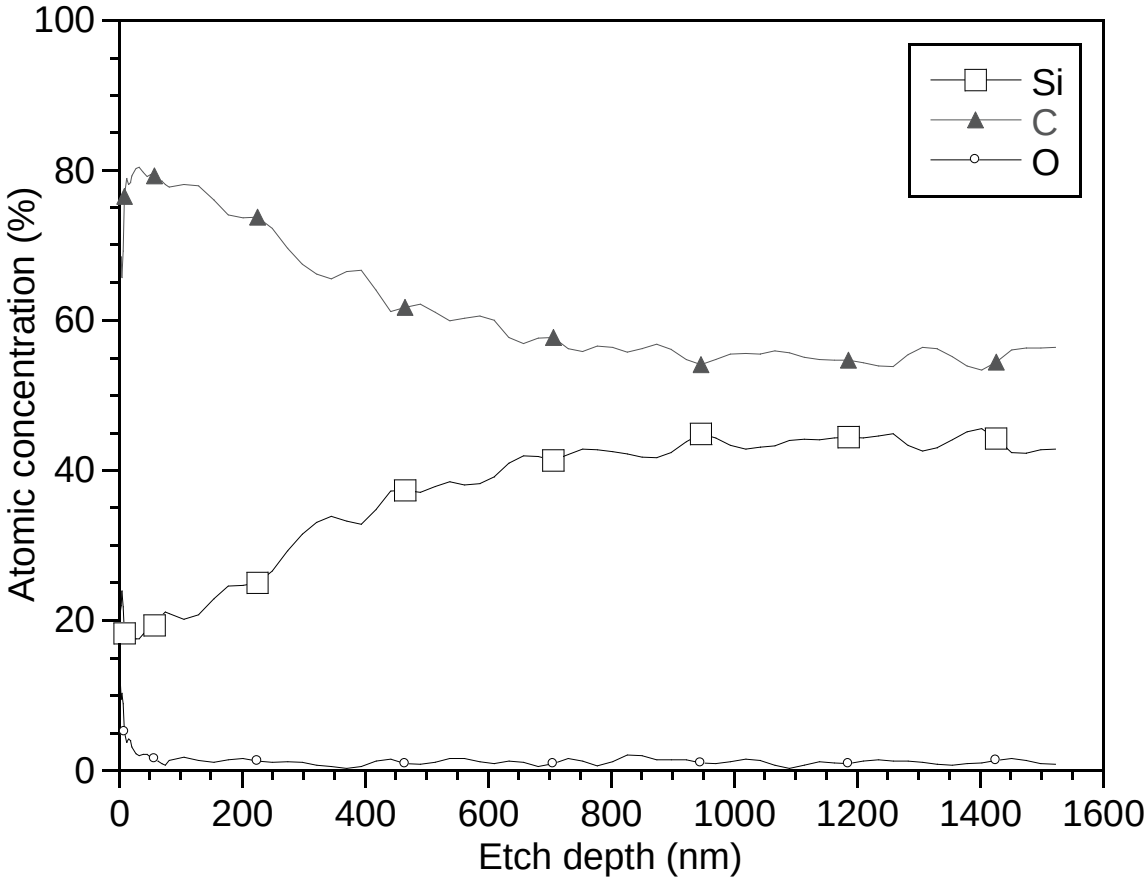

Figure 16 : AES profile of a coating obtained by a decrease of Q_{H2} (from 150 to 0 sccm at a rate -2.5 sccmmin^{-1}, P=5kPa,T=1000°C, Q_{MTS}=50sccm)

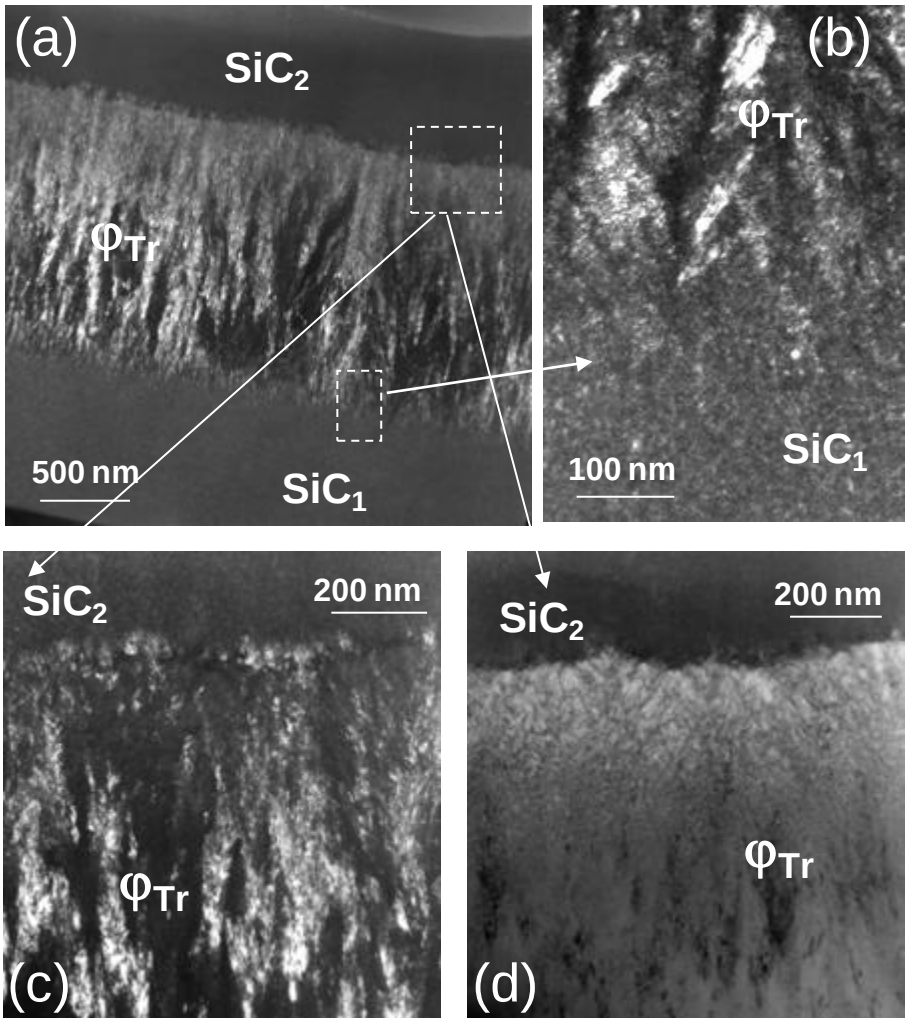

Figure 17a-d : TEM images of a coating obtained by a linear decrease of Q_{H2} (from 150 to 0 sccm at a rate -2.5 sccmmin^{-1}, P=5kPa,T=1000°C, Q_{MTS}=50sccm). (a)-(c) : SiC_{111} dark field, (d) : C_{002} dark field

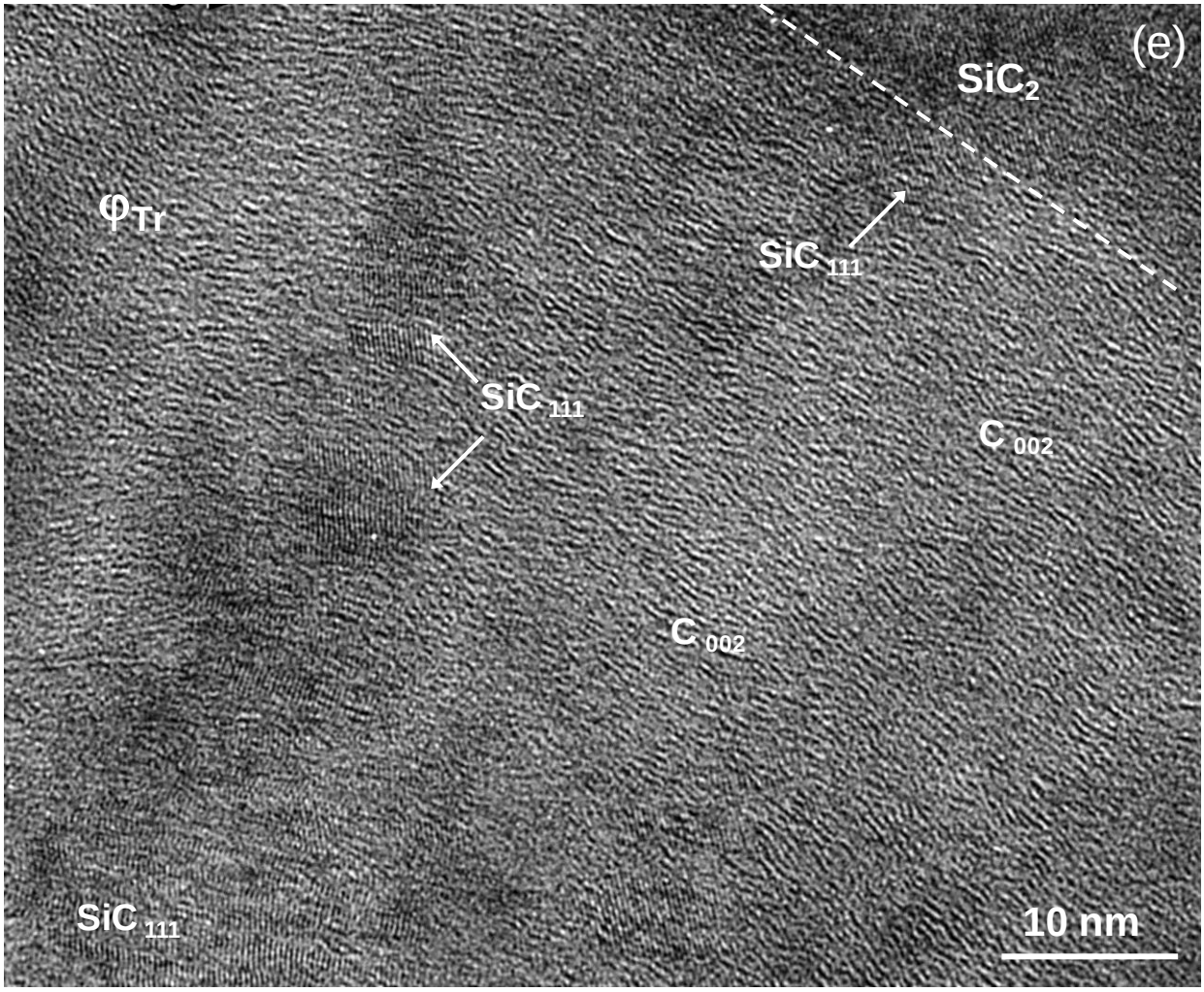

Figure 17e : TEM images of a coating obtained by a linear decrease of Q_{H2} (from 150 to 0 sccm at a rate -2.5 sccmmin^{-1}, P=5kPa,T=1000°C, Q_{MTS}=50sccm). (e) : high resolution.

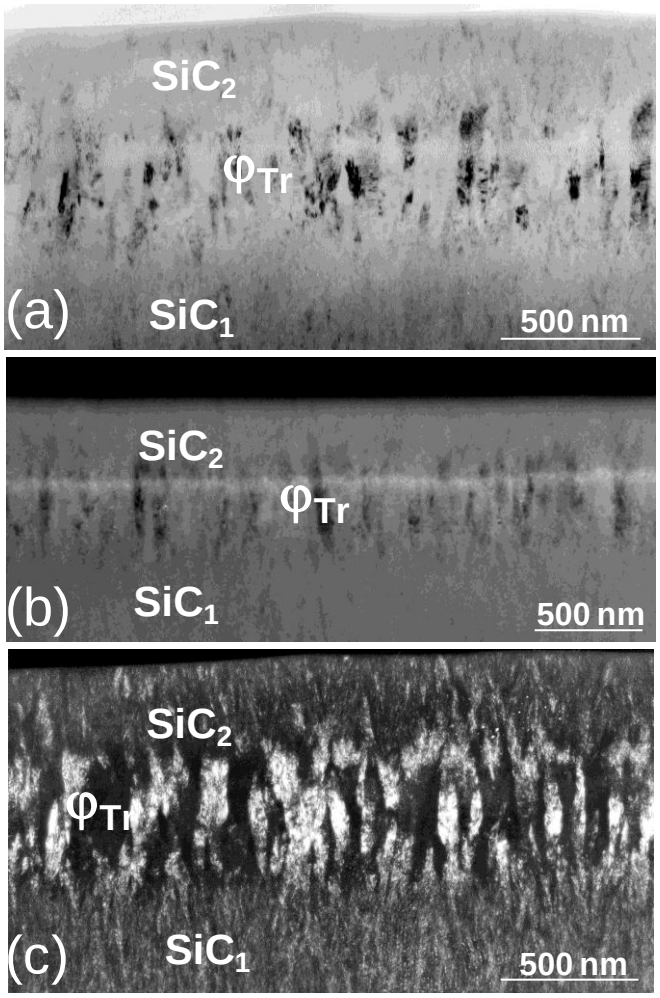

Figure 18: TEM images of a coating obtained by a linear decrease of Q_{H2} (from 150 to 0 sccm at a rate -15 sccmmin^{-1}, P=5kPa,T=1000°C, Q_{MTS}=50sccm). (a) bright field, (b) : C_{002} dark field, (c) SiC_{111} dark field.

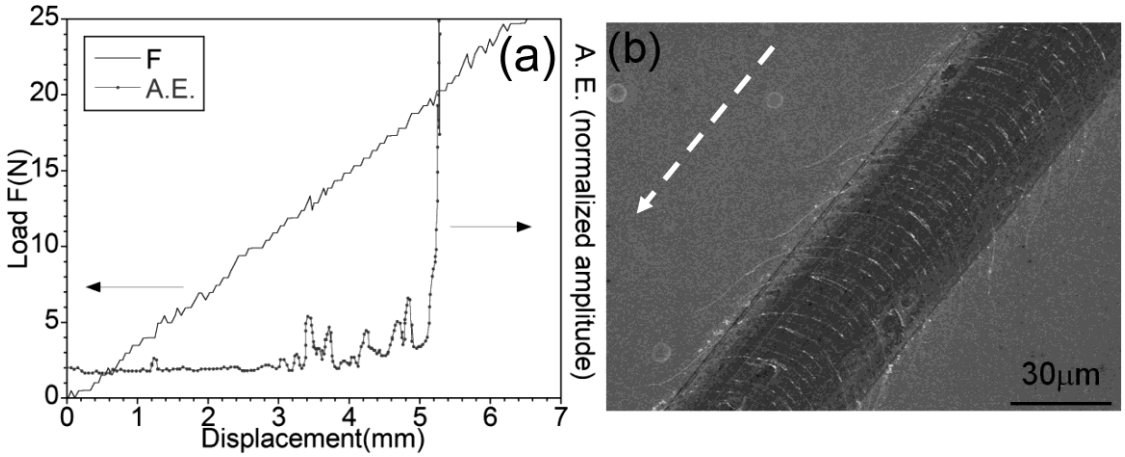

Figure 19 : (a) Load-displacement curve and E.A. signal recorded during the scratch testing of a SiC monolayer (b) morphology of the scratched specimen at F = 12N (white dotted arrow shows the scratching direction).

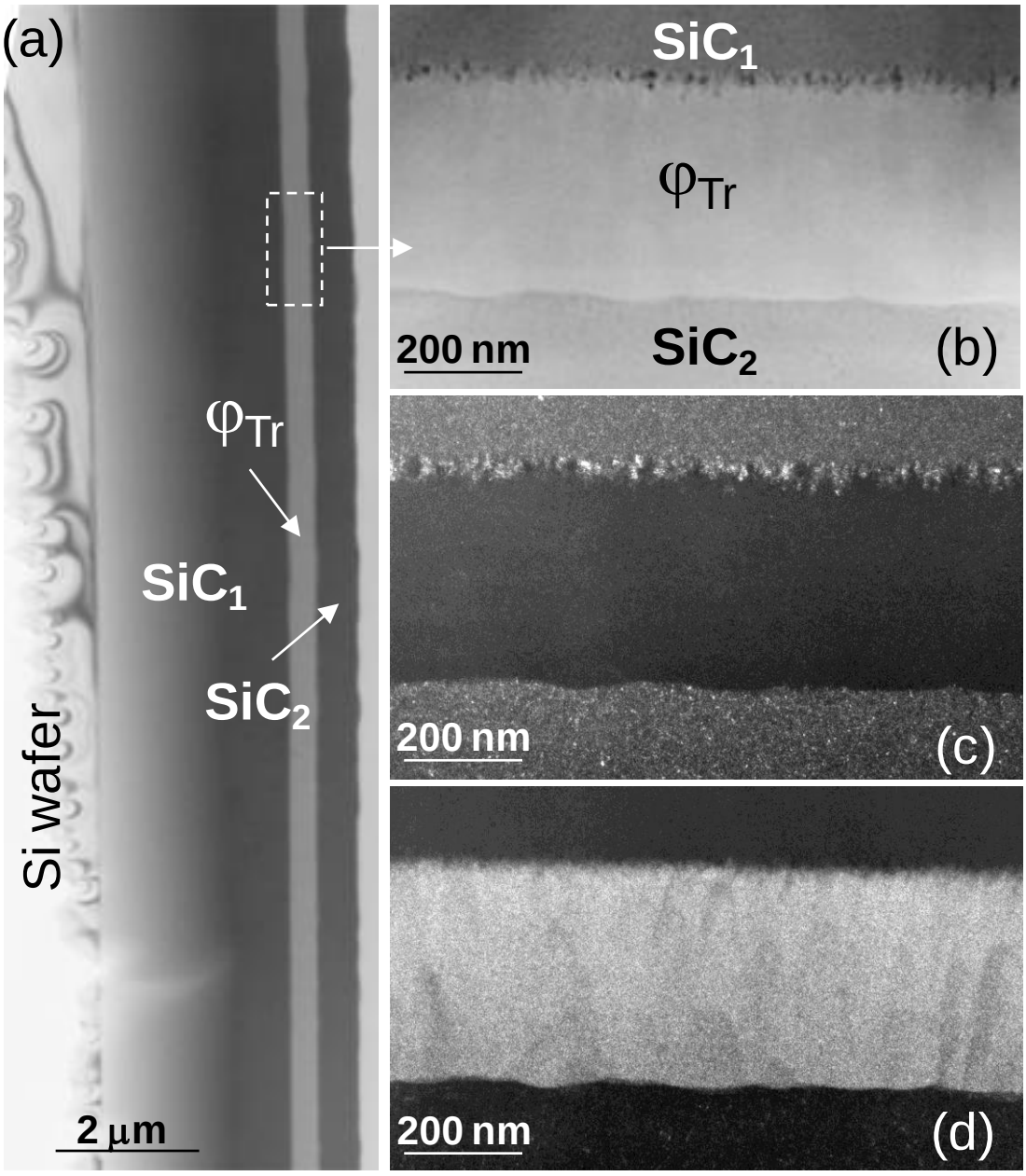

Figure 20 : TEM images of a $SiC_A/\varphi_{Tr}/SiC_B$ bilayer obtained by a steep drop of Q_{H2} (Q_{H2} = 300→0 sccm, P = 5kPa,T = 1000°C, Q_{MTS} = 100sccm, t= 450 s). (a-b) bright field (BF) , (c) SiC_{111}-dark field (DF), (d) C_{002}-DF.

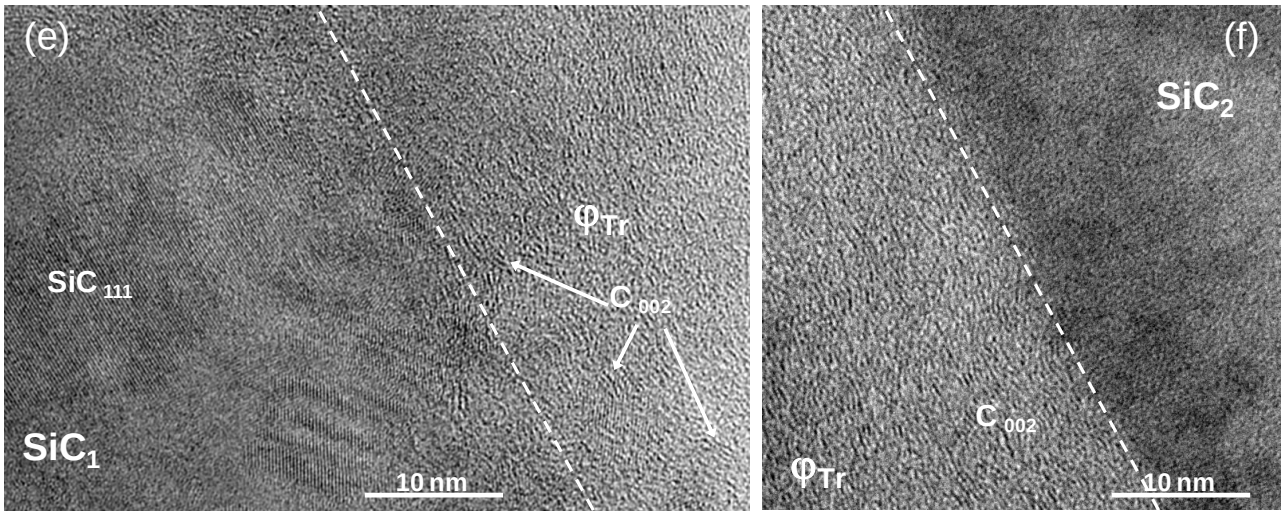

Figure 20 : TEM images of a $SiC_A/\varphi_{Tr}/SiC_B$ bilayer obtained by a steep drop of Q_{H2} (Q_{H2} = 300→0 sccm, P = 5kPa,T = 1000°C, Q_{MTS} = 100sccm, t= 450 s). (e-f) high-resolution (HR).

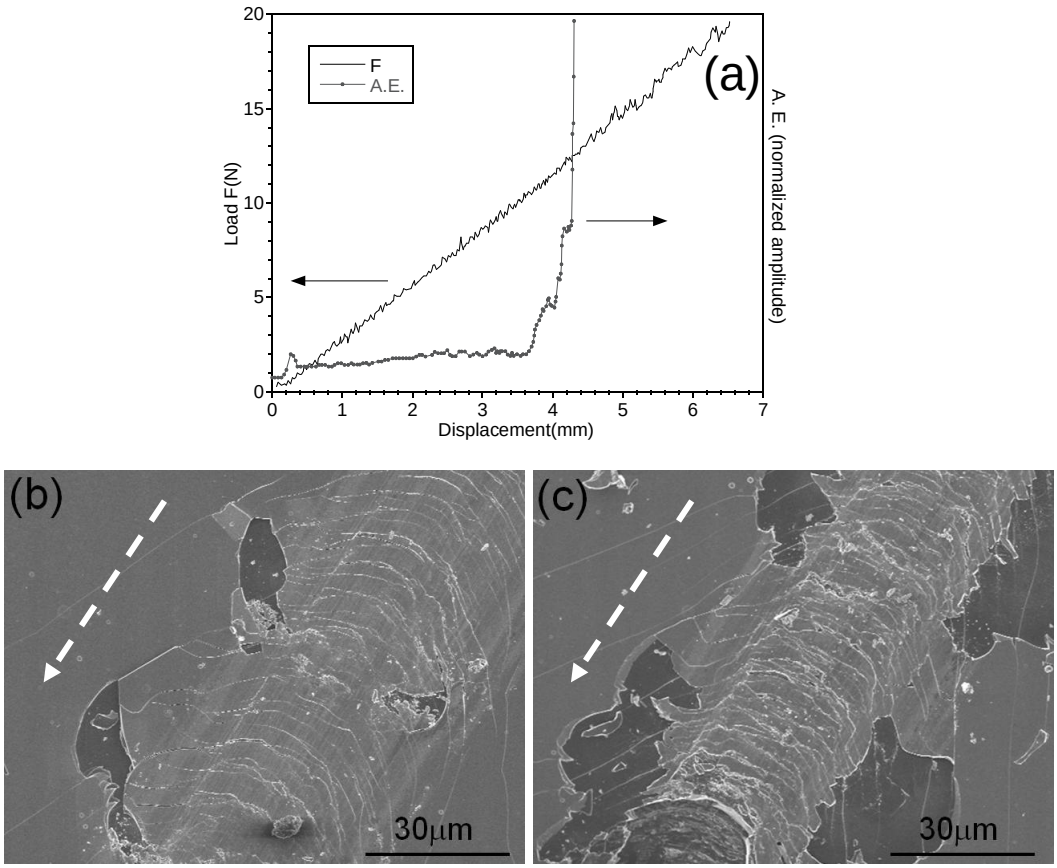

Figure 21 : (a) Load-displacement curve and E.A. signal recorded during the scratch testing of a bilayer with a carbon-rich interphase ($Si/C_{at.}$ = 0.25, $e_{\varphi Tr}$=350nm) (b-c) morphology of the scratched specimen: (b) F=11 N, (c) F= 12 N. (white dotted arrows show the scratching direction).

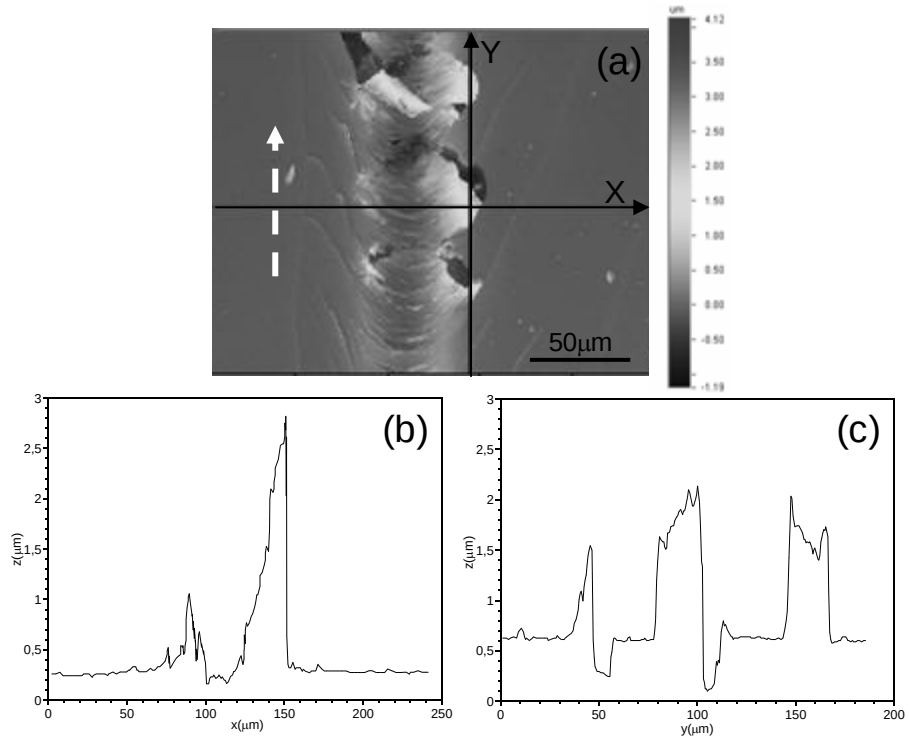

Figure 22 : Topography (from laser profilometry) of a scratched bilayer with a carbon-rich interphase ($Si/C_{at.}$ = 0.25, $e_{\varphi Tr}$ = 350nm) (a) Z mapping, (b) Z profile along X, (c) Z profile along Y. (white dotted arrows show the scratching direction).